1967-12

Phonon and photon paramagnetic resonance lineshapes in ruby

Crooker, Peter Peirce

Monterey, California. U.S. Naval Postgraduate School

PHONON AND PHOTON PARAMAGNETIC RESONANCE LINE-SHAPES IN RUBY

PETER PEIRCE CROOKER

PHONON AND PHOTON PARAMAGNETIC RESONANCE LINESHAPES IN RUBY

by

Peter Peirce Crooker
B.S., Oregon State University, 1959

Submitted in partial fulfillment of the
requirements for the degree of

DOCTOR OF PHILOSOPHY

from the

NAVAL POSTGRADUATE SCHOOL
December 1967

ABSTRACT

Electron paramagnetic resonance (EPR) and acoustic paramagnetic resonance (APR) lineshapes have been measured for four transitions in ruby at 5.924 GHz. Cr concentrations varying from .005% to 1% were used. Second moments were calculated from the APR lines; half-widths were calculated from both EPR and APR lines. A theory is presented which yields the second moment in terms of sums over exchange and dipole-dipole interactions between Cr pairs. It is shown that the theory predicts moments much larger than measured due to the fact that the stronger Cr-Cr interactions lie outside the observed line. A qualitative calculation of the moment from the known interactions supports this conclusion. Finally, half-widths for both APR and EPR lines are compared and shown to be equal.

TABLE OF CONTENTS

LIST OF TABLES

LIST OF ILLUSTRATIONS

ACKNOWLEDGEMENTS

This work would not have been possible without the help of many people and institutions. In particular the author is indebted to:

The Naval Postgraduate School, for the instructorship I occupied during the course of this work.

The Office of Naval Research, who provided the necessary funding.

Prof. E.C. Crittenden, Jr., who introduced me to the subject of magnetic resonance and guided the thesis work.

Prof. O.B. Wilson, Jr., who taught me most of what I now know about microwave equipment.

Dr. Harry Meyer of the Army Missile Command who alerted me to the advantages of resonant transducers.

My fiancée, now wife, Theresa, who gave extensively of her time and patience during the latter stages of the work, and whom I relied upon continually for encouragement and assistance, not the least of which was typing the rough draft of the manuscript.

Finally, to my predecessor on the project, Grady A. Weeks, who was tragically killed during a carrier landing in 1965, this work is respectfully dedicated.

CHAPTER I

INTRODUCTION

If a magnetic ion is placed in a crystal lattice such that it retains all or part of its original magnetic moment, the crystal will display macroscopic magnetic properties. In order to understand these properties, it is necessary first to understand how the magnetic ion interacts with the host lattice, and second, how the ions interact with each other. The technique of electron paramagnetic resonance (EPR), discovered by Zavoisky[1] in 1945, has provided an experimental source from which many of the answers can be found.

In the formative years of EPR, emphasis was placed on the location of paramagnetic resonance lines, i.e., the combination of microwave frequency, static magnetic field, and crystal orientation which would produce resonance absorption of the microwaves. It was obvious, however, that additional information could be derived from the lineshape itself, not only with respect to its width, but also to its mathematical form, especially as it was altered by temperature, crystalline environment, magnetic field direction and magnitude, and ion concentration. Impetus was given to lineshape study by Van Vleck's classic paper[2] in which, rather than attempting the almost impossible problem of calculating the complete lineshape, he showed how to obtain the statistical moments of the line in a simple and direct fashion and how, knowing some of the moments, one could make predictions about the lineshape itself. In particular, Van Vleck showed that the line width is due to the spin-spin interaction between neighboring magnetic ion pairs and that this interaction takes on two forms:

1) Magnetic dipole-dipole coupling which is caused by one ion responding to the magnetic field of another and vice-versa.

2) Exchange coupling resulting from a partial overlap of the wave functions of two ions and causing an apparent spin-spin interaction between the ions.

The result of these mutual perturbations between the ions is to take a large number of exactly coinciding energy levels at, say, E_1, and spread them out into a collection of levels very near E_1. Transitions involving E_1 are consequently spread over a range of energies and the line appears broadened.

Since Van Vleck's paper treated only those ions whose energy levels are completely degenerate at zero magnetic field, Pryce and Stevens[3] were able to extend the treatment to cases where the crystalline electric field caused the levels to be initially split. In this case, the levels are not equidistant and Van Vleck's approach must be modified accordingly. Pryce and Stevens' results are especially significant: for their case, the exchange interaction contributes sizeably to the second moment, whereas in the Van Vleck case, exchange appears only in the experimentally less accessible higher moments. Ishiguro, Kambe, and Usui[4] have exploited this fact in an analysis of EPR lineshapes in nickel fluosilicate; their success has been a strong motivating factor for the present study. We will develop Pryce and Stevens' result in more detail in a later section; suffice us now to say that a measurement of the second moment of a line can yield much information concerning the exchange forces between neighbors.

Late in the 1950's, a new technique appeared for the investigation of paramagnetic ions in crystals. Called acoustic paramagnetic resonance (APR), the method is in many ways similar to EPR. Typically, a high frequency ($\nu \sim 10$ GHz) acoustic pulse is applied to one end of a paramagnetic crystal and allowed to reflect from the other end. The height of this return echo is then monitored as a large static magnetic field B is slowly varied. At the resonance value of B, the echo diminishes sharply; here, the interpretation is that the energy levels of the crystal have been shifted by B until there exists a pair with energy separation equal to $h\nu$ for the sound. This particle of sound, which is analogous to the photon of EPR, is called a phonon. Photons and phonons are not identical in their interaction with ions, however, for the energy field-atom interaction is quite different. Classically, EPR occurs because the atom has a magnetic dipole which responds to the microwave field's magnetic induction H; quantum mechanically, this leads to selection rules of $\Delta m = 0$ or $\Delta m = \pm 1$, depending on the polarizations involved. On the other hand, APR is caused by a lattice wave, periodically modulating the crystalline electric field environment of the paramagnetic ion. Since the atom's wave function is very sensitive to its environment, its orbital angular momentum L responds to the lattice and, by the mechanism of L-S coupling, the sound wave finds itself ultimately modulating the electronic spin S. The perturbation is quadrupolar in nature and, as we will show in detail later, can lead to selection rules of $\Delta m = 0, \pm 1, \pm 2$. Not only is it possible to see different transitions with APR than with EPR, but if there is a mixing of the

m-states, such as when the magnetic field differs from the quantization axis, we will see a different blend of transitions between the same two energy levels.

The basic APR technique was developed experimentally by Jacobsen, Shiren, and Tucker;[5] the theoretical basis was developed in a series of papers by Altshuler and summarized in a review article by Altshuler, Kochelaev, and Leushin.[6] The latter paper also gives a summary of the rather limited theoretical status of APR lineshapes. For transitions of $\Delta m = \pm 1$, one can show that the second moment is exactly equal to that for EPR; but for $\Delta m = \pm 2$, the two moments are significantly different. For the fourth moments of EPR and APR in the Van Vleck case, (i.e., no zero magnetic field splitting), London[7] has shown that they are nearly the same; thus, comparing second and fourth moments, the APR line should be wider. No fourth moments have been calculated for atoms whose energy levels have undergone crystalline field splitting. More work is necessary in this direction.

The fact that APR and EPR lineshapes may differ seems to be a little exploited fact. It is of interest to know specifically what causes the shape changes and if these changes also occur for atoms with crystal field splitting. Meyer, et. al.,[8] have reported preliminary data on ruby but their study appears to have been terminated in the literature. The only other work, to our knowledge, is that of Weeks[9] at the Naval Postgraduate School. His results form the initial phase of the present study.

In this paper, we develop a theory for the second moments of both acoustic and photon resonance lines, following the prescription given by Pryce and Stevens.[3] We then show how to apply the theory to the case in which the magnetic field is at an arbitrary angle to the crystal axes and we explicitely evaluate second moments for ruby in terms of exchange and magnetic dipole-dipole strengths. It will turn out that the second moments for EPR and APR lines are identical, but that there is an angular dependence resulting from mixing of the energy states when the applied magnetic field is not parallel to the crystal c-axis.

We have also performed experiments on rubies of concentration varying from .005% to 1% by weight, measuring both the acoustic and photon lineshapes of several transitions. Halfwidths are presented for both sets of lines, and moments are calculated from the acoustic lines.

Finally, we compare experimental and theoretical moments, discover that the two do not agree, and present an explanation why agreement is difficult to expect. We also discuss the halfwidths of both sets of lines.

CHAPTER II

GENERAL THEORY

The technique for obtaining the statistical moments of a magnetic resonance line originated with Van Vleck,[2] who showed that while the precise shape of the line is prohibitively difficult to determine, the invariance of diagonal sums in quantum mechanics allows a straightforward calculation of the line's moments. The theory was soon expanded in several directions: Kittel and Abrahams[10] treated the case where the paramagnetic ions were dilute, being an impurity added to a host crystal; Kambe and Usui[11] included the temperature dependence of the moments; and Pryce and Stevens[3] derived formulas for ions whose energy levels are initially split by a crystalline field. More recently, McMillan and Opechowski[12] have incorporated these refinements into one set of formulas. In this section, we will rederive the expression for second moments, following essentially the approach of Pryce and Stevens. It will be seen that the inclusion of phonon induced transitions does not alter the theory in any way and that the results apply in a natural way to APR.

We start by supposing a large number of paramagnetic ions in a host lattice, such that each ion is characterized by an identical set of R energy levels in the absence of any ion-ion coupling. Two of these levels, it will be further supposed, are separated by energy $h\nu_o$; it is the width of the transitions between these levels that we wish to calculate. To do this, consider the quantum states $|\alpha\rangle$ of the entire crystal; under

the assumption of no coupling, these are just products of single ion states, so that the energy E_α is characterized mainly by a certain number of ions in each single ion energy level. Of course, since there are numerous ways to achieve a given system energy, $|\alpha\rangle$ is highly degenerate, containing as it does all possible spin combinations yielding the energy E_α. Now, if one of the ions in $|\alpha\rangle$ absorbs a photon or phonon of energy $h\nu_o$, then the crystal goes into a new quantum state $|\beta\rangle$ of energy $E_\beta = E_\alpha + h\nu_o$ which is also highly degenerate. In this model, we therefore see that the resonance line is discrete at $h\nu_o$ and no broadening occurs.

We next introduce a small inter-ion coupling $W = \Sigma W_{ij}$, where the summation is over all ion pairs i and j. The effect of W on the degenerate states of $|\alpha\rangle$ is to introduce a number of off-diagonal terms in the Hamiltonian matrix; we then rediagonalize and end up with new states $|a\rangle$ formed from linear combinations of the zero order states. The outcome of this process is to lift the degeneracy of the zero order states $|a\rangle$, so that the energy $E_a = E_\alpha + \langle a|W|a\rangle$. The original energy level has thus been smeared out into a very large number of closely spaced levels; our resonance line is no longer discrete at $h\nu_o$ but is, instead, an amalgamation of transitions from the set of levels $|a\rangle$ near E_α to the set of levels $|b\rangle$ near E_β, all of which appear as a broad transition at $h\nu_o$.

We can now write down the formula for the absorption $A(\nu)$ between states $|a\rangle$ and $|b\rangle$. It is

$$A(\nu) = \text{(no. of transitions up)} - \text{(no. of transitions down)}$$

$$\propto (n_a - n_b)(E_b - E_a)\left|\langle a|M|b\rangle\right|^2 \delta(h\nu - E_b + E_a)$$

$$\propto \frac{\left(e^{-E_a/kT} - e^{-E_b/kT}\right)(E_b - E_a)\left|\langle a|M|b\rangle\right|^2 \delta[\nu - (E_b - E_a)/h]}{\sum_s e^{-E_s/kT}}$$

where n_a and n_b are the populations of levels a and b, $\left|\langle a|M|b\rangle\right|^2$ is the matrix element of an arbitrary transition inducing operator M, $e^{-E_s/kT}$ is the usual Boltzmann factor, the sum in the denominator is the partition function over all possible levels E_s, and $\delta[\nu - (E_b - E_a)/h]$ is a delta function at $h\nu = E_b - E_a$. If it were possible to determine the states $|a\rangle$ and $|b\rangle$, we could sum this expression over those states $|a\rangle$ and $|b\rangle$ that determine the strength of the line at ν; practically speaking, this is virtually impossible since then we would have to know all the mixings of the zero order states of $|\alpha\rangle$ and $|\beta\rangle$. If we settle for sums over <u>all</u> states $|a\rangle$ and $|b\rangle$, however, this amounts to taking the trace of the Hamiltonian matrix, which can be done using the zero order states. It is this fact that makes moment calculations possible.

First we make some simplifying approximations with respect to the temperature. We write the expression

$$\left(e^{-E_a/kT} - e^{-E_b/kT}\right)(E_b - E_a)$$

as

$$e^{-E_\alpha/kT}\, e^{-\langle a|W|a\rangle/kT}\left[1 - e^{-(h\nu_o + \langle b|W|\rangle - \langle a|W|a\rangle)/kT}\right]$$

$$X\left[h\nu_o + \langle b|W|b\rangle - \langle a|W|a\rangle\right]$$

Since $\langle b|W|b\rangle$ and $\langle a|W|a\rangle$ are much less than $h\nu_o$ we drop them where they appear as terms and get

$$\left(e^{-E_\alpha/kT} \; e^{-\langle a|W|a\rangle/kT} \right)_{h\nu_o} \left(1 - e^{-h\nu_o/kT} \right)$$

A next approximation is to assume $\langle a|W|a\rangle \ll kT$ and replace $\exp(-\langle a|W|a\rangle/kT)$ by unity; this is not very restrictive at all since $\langle a|W|a\rangle$ is quite small. We are thus left with

$$A(\nu) \propto \left[\frac{h\nu_o \left(1 - e^{-h\nu_o/kT}\right)}{\sum_s e^{-E_s/kT}} \right] e^{-E_\alpha/kT} \; |\langle b|M|a\rangle|^2 \; \delta\left[\nu - (E_b - E_a)/h\right]$$

and since the factor in brackets is just a constant, we drop that too. In any case, we will ultimately take ratios of the above expression so that the bracketed factor will cancel out.

We now define the lineshape $g(\nu)$ of the resonance line at ν_o:

$$g(\nu)d\nu = \frac{\sum_{a,b}^{\Delta} e^{-E_\alpha/kT} \; |\langle a|M|b\rangle|^2 \; \delta\left[\nu - (E_b - E_a)/h\right]}{\sum_{a,b} e^{-E_\alpha/kT} \; |\langle a|M|b\rangle|^2 \; \delta\left[\nu - (E_b - E_a)/h\right]}$$

where the upper summation is taken over just those a,b pairs such that $h\nu \leq (E_b - E_a) \leq h(\nu + d\nu)$ and the lower summation is over all possible pairs. In fact, the denominator is just the area of the line. The moments can be defined in terms of $g(\nu)$ as follows:

$$\langle \Delta\nu^n \rangle = \int_o^\infty (\nu - \nu_o)^n \; g(\nu)d\nu$$

$$= \frac{\sum_{a,b} e^{-E_\alpha/kT} \; (E_b - E_a)^n \; |\langle a|M|b\rangle|^2}{\text{area}}$$

where now the summation is over all pairs.

In order to evaluate this, we first put it in the form of a trace; the introduction of projection operators P_α and P_β will greatly simplify the form. We define P_α by[13]

$$P_\alpha = \sum \quad |a\rangle \langle a| \qquad \text{sum over all } |a\rangle \text{ in } |\alpha\rangle$$

so that P_α applied to any state selects out only those in the manifold $|\alpha\rangle$. These operators will be useful in keeping track of the states when we perform the traces. For instance, the area can now be written

$$\text{area} = \sum_{a,b} e^{-E_\alpha/kT} \langle a|M|b\rangle \langle b|M|a\rangle$$

$$= \sum_{a} e^{-E_\alpha/kT} \langle a|P_\alpha M P_\beta M|a\rangle$$

and we have a trace. The first moment involves the expression

$$X = \sum_{a,b} e^{-E_\alpha/kT} (E_b - E_a) \, |\langle a|M|b\rangle|^2$$

$$= \sum_{a,b} e^{-E_\alpha/kT} (\langle b|W|b\rangle - \langle a|W|a\rangle)\langle a|M|b\rangle \langle b|M|a\rangle$$

$$= \sum_{a} e^{-E_\alpha/kT} \langle a|P_\alpha M P_\beta W P_\beta M - P_\alpha M P_\beta M P_\alpha W|a\rangle,$$

and finally the second moment involves

$$Y = \sum_{a,b} e^{-E_\alpha/kT} (E_b - E_a)^2 \, |\langle a|M|b\rangle|^2$$

$$= \sum_a e^{-E_\alpha/kT} \langle a | P_\alpha M P_\beta W P_\beta W P_\beta M + P_\alpha W P_\alpha W P_\alpha M P_\beta W$$

$$- 2 P_\alpha M P_\beta W P_\beta M P_\alpha W | a \rangle$$

The evaluation of these traces is a tedious but straightforward process. We start by invoking one more approximation: that of setting $\exp(-E_\alpha/kT)$ equal to unity. Our results are therefore restricted to moderately high temperatures, but the calculations are considerably simplified. Retention of the exponential factor is the basis of the temperature studies mentioned earlier.

We will use the following notation in what follows:

$M = \sum_i M_i$: sum over all ions i

$W = \frac{1}{2} \sum'_{k\ell} W_{k\ell}$: sum over all ions k, ℓ, but not $k = \ell$

$|a\rangle = |a_1, a_2, \cdots a_n\rangle$: $|a_i\rangle$ = one of R single-ion states

The expression for $|a\rangle$ is now in the uncoupled representation; this is permissable because we are going to calculate a trace. First, we calculate the area.

$$\text{area} = \sum_a \langle a | P_\alpha M P_\beta M | a \rangle$$

$$= \sum_p \sum_q \sum_a \langle a_1 a_2 \cdots a_p \cdots a_q \cdots a_n | P_\alpha M_p P_\beta M_q | a_1 \cdots a_p \cdots a_q \cdots a_n \rangle$$

$$= \sum_p \sum_q \sum_{a_1} \langle a_1 | a_1 \rangle \cdots \sum_{a_p} \sum_{a_q} \langle a_p a_q | P_\alpha M_p P_\beta M_q | a_p a_q \rangle \cdots$$

The sums $\sum_{a_i} \langle a_i | a_i \rangle$ are just $\sum_{a_i=1}^{R} (1) = R$, but the sum over a_p and a_q is slightly more complicated. Because of P_α, $|a_p a_q\rangle$ must be in the P_α manifold, so that either ion p or q must be in the

lower state of our transition. If we call the two levels of the transition 1 and 2, then $|a_p a_q\rangle = |1a_q\rangle$, $|a_p 1\rangle$ or $|11\rangle$; if this were not true, then P_α acting back on $\langle a_p a_q|$ would yield zero. Now there are two cases: either $p \neq q$ or $p = q$. In the former case, we have only the three possibilities

$$\langle 11|P_\alpha M_p P_\beta M_q|11\rangle \to \langle 11|M_p|12\rangle \to \langle 11|22\rangle = 0$$

$$\langle 12|P_\alpha M_p P_\beta M_q|12\rangle \to \langle 12|M_p P_\beta|11\rangle = 0$$

$$\langle 21|P_\alpha M_p P_\beta M_q|21\rangle \to \langle 21|M_p|22\rangle \to \langle 21|12\rangle = 0$$

so that these terms all vanish. Next we try $p = q$; we get

$$\sum_{a_p} \langle a_p|a_p\rangle \sum_{a_q} \langle 1|P_\alpha M_p P_\beta M_p|1\rangle = R\,|\langle 1|M_p|2\rangle|^2$$

The total area is therefore

$$\text{area} = \sum_p R^{N-1}\,|\langle 1|M_p|2\rangle|^2 = NR^{N-1}|\langle 1|M_p|2\rangle|^2$$

Notice that the form of M_p is unimportant; all that matters is that it connects the two states $|1\rangle$ and $|2\rangle$.

We next calculate the second moment, although in less detail since the procedure is identical. The expression has three terms, the first of which is

$$X = \sum_a \langle a|P_\alpha M P_\beta W P_\beta W P_\beta M|a\rangle$$

$$= \tfrac{1}{2} \sum_{ij}{}' \tfrac{1}{2} \sum_{k\ell}{}' \sum_{pq} \sum_a \langle a_1 \cdots a_n|P_\alpha M_p P_\beta W_{ij} P_\beta W_{k\ell} P_\beta M_q|a_1 \cdots a_n\rangle$$

It turns out that the only non-vanishing possibility here is

$$X = \tfrac{1}{2} \sum_{ij}{}' \sum_{a_1} \langle a_1|a_1\rangle \cdots \sum_{a_i} \sum_{a_j} \langle a_i a_j|P_\alpha M_s P_\beta W_{ij} P_\beta W_{ij} P_\beta M_t|a_i a_j\rangle \cdots$$

where s and t = i or j. Although all the substitutions of i and j for s and t must now be considered, we display just one:

$$Z = \langle 11|P_\alpha M_i P_\beta W_{ij} P_\beta W_{ij} P_\beta M_j|11\rangle$$

$$= \langle 1|M_i|2\rangle \langle 21|W_{ij} P_\beta W_{ij}|12\rangle \langle 2|M_j|1\rangle$$

$$= \langle 1|M_i|2\rangle \langle 2|M_j|1\rangle \left[\langle 21|W_{ij}|12\rangle \langle 12|W_{ij}|12\rangle + \langle 21|W_{ij}|21\rangle\langle 21|W_{ij}|12\rangle\right]$$

The evaluation of the other possibilities for s and t and of the other terms in the moment can be performed in similar fashion. Since there are no new assumptions or techniques, we proceed directly to the answer. It is

$$h^2\langle \Delta\nu^2\rangle = \frac{1}{NR} \sum_{ij}' \left|\langle 11|W_{ij}|11\rangle - \langle 21|W_{ij}|21\rangle - \langle 21|W_{ij}|12\rangle\right|^2$$

$$+ \left|\langle 22|W_{ij}|22\rangle - \langle 12|W_{ij}|12\rangle - \langle 21|W_{ij}|12\rangle\right|^2$$

$$+ \sum_{s=3}^{R} \left|\langle 1s|W_{ij}|1s\rangle - \langle 2s|W_{ij}|2s\rangle\right|^2$$

$$+ \left|\langle 1s|W_{ij}|s1\rangle - \langle 2s|W_{ij}|s2\rangle\right|^2$$

where we have divided by the area and thereby lost the interaction matrix elements. This is the general expression for the second moment.

Before we close this section, we make a general comment on the form of W_{ij}. If one writes down W_{ij} for magnetic dipole interactions, one finds a number of diagonal terms and a number of off-diagonal terms. The effect of the diagonal terms is to mix the states of P_α

states among the P_β and other states. In the latter case, we could then have transitions between states where $E_\beta - E_\alpha = 0, 2h\nu_o, 3h\nu_o$, etc., and our moments would include their areas. Since our measurement is confined to the neighborhood of $h\nu_o$, however, we must incorporate this situation into the theory, namely by truncating W_{ij} to only the diagonal part. This step is not an approximation but rather a requirement for obtaining the correct answer. Explicitly how the truncation is carried out will be discussed in the next section, when we apply our general formula to the specific case of ruby.

CHAPTER III

APPLICATION TO RUBY

We next apply our theory to the particular case of ruby. We have chosen ruby for several reasons:

1. The ruby crystal structure and energy spectrum are well known. Both energy levels and state coefficients have been tabulated as functions of magnetic field angle and are readily available in the literature.
2. Ruby is commercially available in many synthetic forms due to its popularity as a laser crystal. It is extremely hard and may be polished to a high degree of accuracy--an important point when considering acoustic techniques.
3. Finally, the ruby lineshape has been a puzzle to many workers over the years. We will review this previous work in a later section.

Ruby is aluminum oxide ($Al_2 O_3$) in which some of the Al ions have been isomorphically replaced by Cr ions in the trivalent state. The lattice symmetry is rhombohedral and belongs to the space group D^6_{3d} with four and six sites in the unit cell for aluminum and oxygen atoms, respectively.[14] Figure 3-1 shows the location of the aluminum ions in the unit cell; since we will only use the aluminum sublattice, we have left out the oxygens for simplicity. The edge of the cell is a = 5.128A in length and the apex angle is $\alpha = 55.33^{o}$.

A simpler way of looking at this lattice is as a slightly distorted hexagonal close packing of oxygens, with aluminums filling some of the interstices and the c-axis parallel to the trigonal axis of the rhombohedral unit cell. The close packing would be perfect

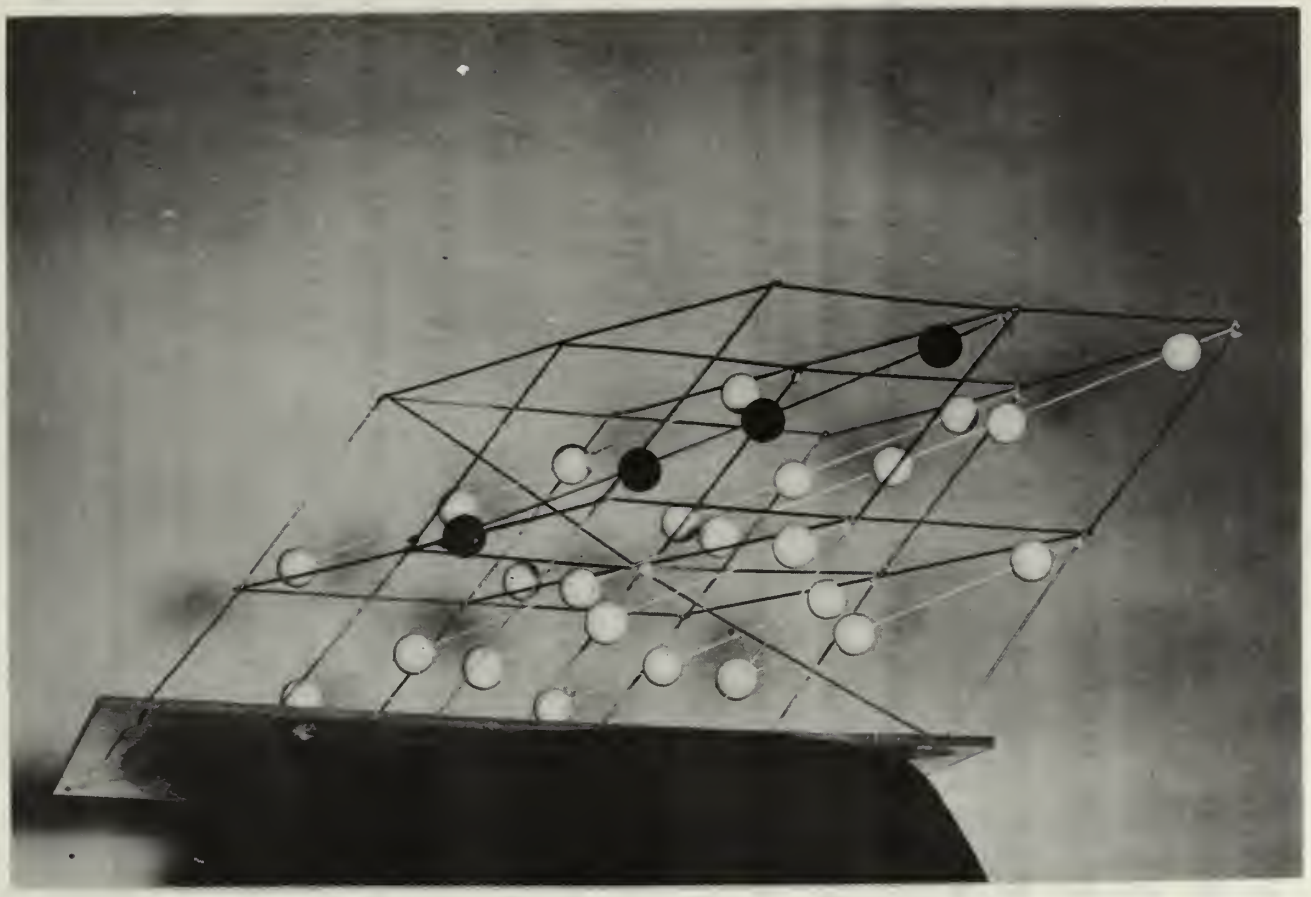

Figure 3-1. Model of Al sublattice in Al_2O_3. The black balls, lying on c-axis belong to one unit cell out of the eight unit cells shown. Apex angle of the rhombohedral unit cell is 55.33^o; the side is 5.128A.

if the rhombohedral apex angle were $53^{o}47'$ and the trigonal coordinates of the aluminum were a/3 instead of .3475 a; nevertheless, we can get a good idea of the lattice if we view it as being purely hexagonal. Figure 3-2 shows a gum drop model constructed in this spirit, exhibiting the aluminum sublattice both with and without the oxygens. The first five neighbors, with which we shall concern ourselves later, are also indicated in Fig. 3-2.

A free Cr^{3+} ion has a $3d^3$ electronic configuration and a $4F_{3/2}$ ground state. The Al site which the Cr ion occupies in ruby is surrounded by a slightly distorted octohedron of oxygen ions. Weeks[9] has discussed the group theoretical aspects of determining the energy levels of the Cr^{3+} ion under the influence of the crystalline field. For our purposes, it is sufficient to know that the angular momentum of the ion is quenched and an effective spin S = 3/2 describes the four resulting levels. These levels are not all degenerate but consist of two Kramers doublets: the lower doublet corresponds to $S_z = \pm 3/2$; the upper corresponds to $S_z = \pm 1/2$ and lies 11.5 GHz above the lower doublet.[15] Upon the application of a magnetic field, the doublet degeneracies are resolved and four non-equidistant levels appear, but the details of the splitting are dependent on the magnetic field direction.

The meeting point between theory and experiment in a paramagnetic resonance experiment is usually the so-called spin Hamiltonian[16]; we now use this device to further describe the behavior of Cr^{3+} in Al_2O_3. Leaving out spin-spin interactions until later, the spin Hamiltonian is

$$\mathcal{H} = \beta(g_{\perp} S_x H_x + g_{\perp} S_y H_y + g_{\parallel} S_z H_z) - D(S_z^2 - \tfrac{1}{3} S(S+1))$$

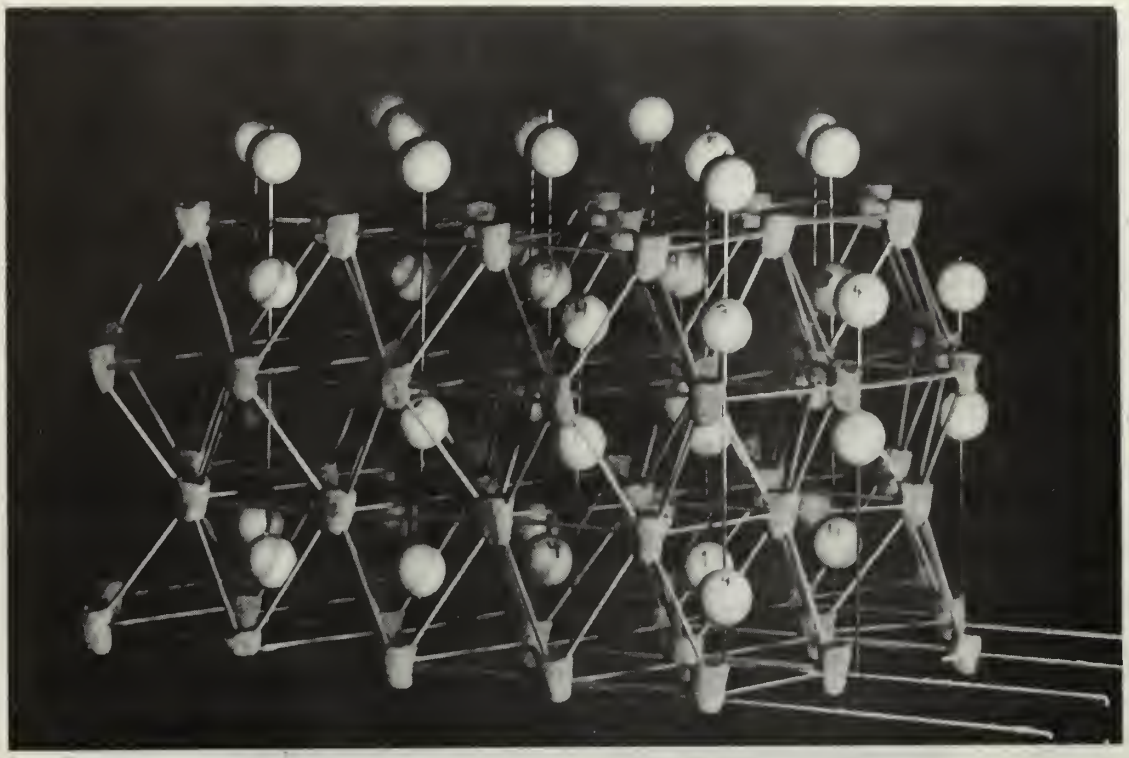

Fig. 3-2a. Al sublattice of Al_2O_3 (white balls) with surrounding oxygen sublattice (gum drops).

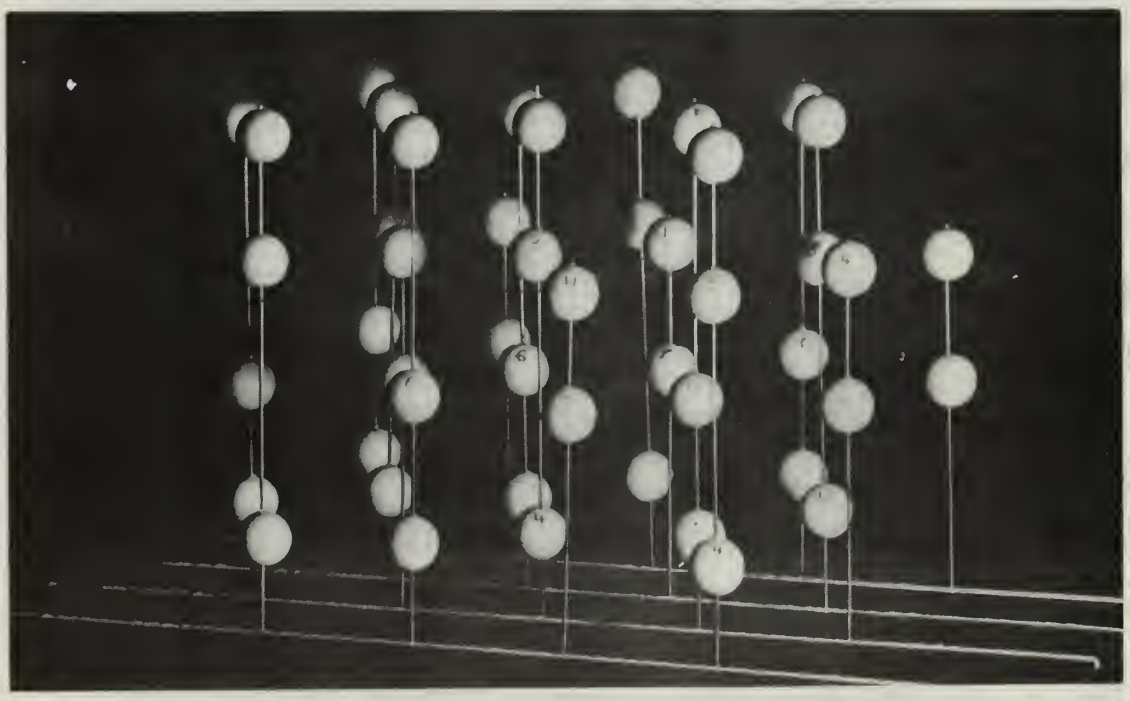

Fig. 3-2b. Al sublattice only. Atoms are approximately in horizontal planes. Neighbors of atom 0 are numbered 1 through 6.

where $g_\perp$ and $g_{||}$ are the perpendicular and parallel g-factors, β is the Bohr magneton, (H_x, H_y, H_z) the applied magnetic field components, (S_x, S_y, S_z) the spin operators, S = 3/2, and D is the crystal field parameter. The values[15] of g are $g_{||} = 1.9840$ and $g_\perp = 1.9867$; the value[17] of D is 5.75 GHz. Inasmuch as $g_\perp \simeq g_{||}$ we will be able to use the value $g_\perp = g_{||} = 2.00$ in all our calculations with negligible loss in accuracy. Thus,

$$\mathcal{H} = g\beta \vec{H} \cdot \vec{S} - D(S_z^2 - \frac{15}{4})$$

where we have substituted 3/2 for S. The axes are rigidly fixed in the crystal with the z-axis parallel to the trigonal axis.

The method of solving this expression for the energy levels is to form matrix elements of $\mathcal{H}$ with the pure spin states of S—for example $\langle m = \frac{3}{2} \mid \mathcal{H} \mid m = \frac{1}{2} \rangle$-- and from the matrix elements, form a 2S + 1 square matrix. If the matrix is already diagonal, such as when $H = H_z$, then the energy levels correspond to the diagonal values, one for each pure state. If, however, H_x and/or H_y is non-zero, the Hamiltonian matrix will contain off-diagonal contributions from the S_x and S_y operators. Then, the matrix must be rediagonalized, the pure state vectors will be mixed together, and the energies themselves will be different from the previous case. A typical level is then described as being in the state $|a\rangle = a_1|\frac{3}{2}\rangle + a_2|\frac{1}{2}\rangle + a_3|-\frac{1}{2}\rangle + a_4|-\frac{3}{2}\rangle$, which is a linear combination of the pure states.

For the above spin Hamiltonian as applied to ruby, Siegman[18] has published values of the energy levels versus magnetic field in 10° intervals from 0° to 90°. He has also listed the state coefficients (the a_j's in the above example) for each level and the

probabilities for EPR transitions between any pair of levels. We have plotted two representative energy level diagrams in Fig. 3-3. Figure 3-3a shows the levels when H is parallel to the c-axis of the crystal; each level is a pure state as shown. Figure 3-3b is for H at 50° to the c-axis; to show the mixing, we have explicitely written out one state function.

Next, we turn to the question of which transitions are observable in our resonance experiments. The first condition that must be met is that the separation between two levels corresponds to $h\nu$, where ν is the microwave or sound frequency. We have plotted the H-θ combinations which will yield resonance for our frequency of ν = 5.924 GHz in Fig. 3-4. However, even if the energy spacing criterion is met, the transition may still be unobservable unless we satisfy a second condition: the transition strength must be large enough to be observable. Transition probabilities are determined from the rule,

$$W = \frac{2\pi}{\hbar} |\langle a|\mathcal{H}_{int}|b\rangle|^2 g(E)$$

where $\hbar$ = Planck's constant/2π, $|a\rangle$ and $|b\rangle$ are the two levels involved in the transition, $\mathcal{H}_{int}$ is the interaction Hamiltonian between the perturbing field and the paramagnetic ion, g(E) is the lineshape (in units of energy^{-1}) having area normalized to unity, and W is the transition probability per unit time (in sec^{-1}). If the interaction has the form $\mathcal{H}_{int}$ = A cos ωt then the transition probability becomes

$$W = \left(\frac{2\pi}{h}\right)^2 |\langle a|A|b\rangle|^2 g(\nu)$$

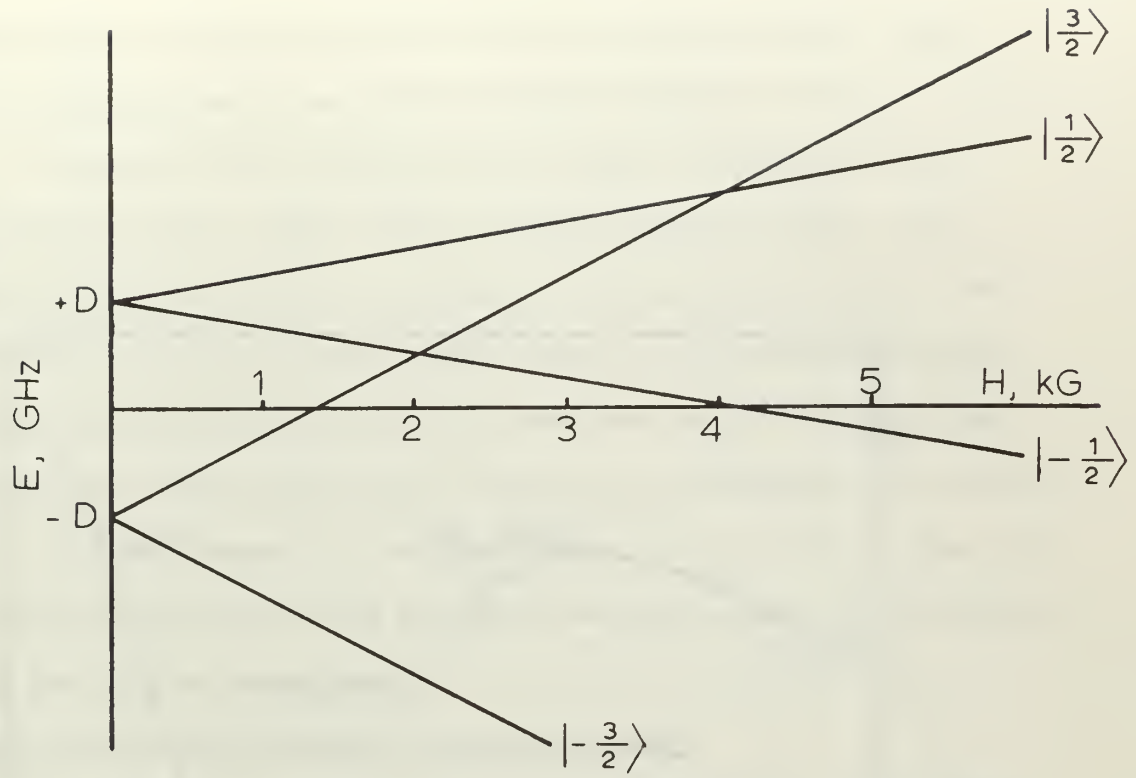

Fig. 3-3a. Energy levels of ruby for H parallel to c-axis.

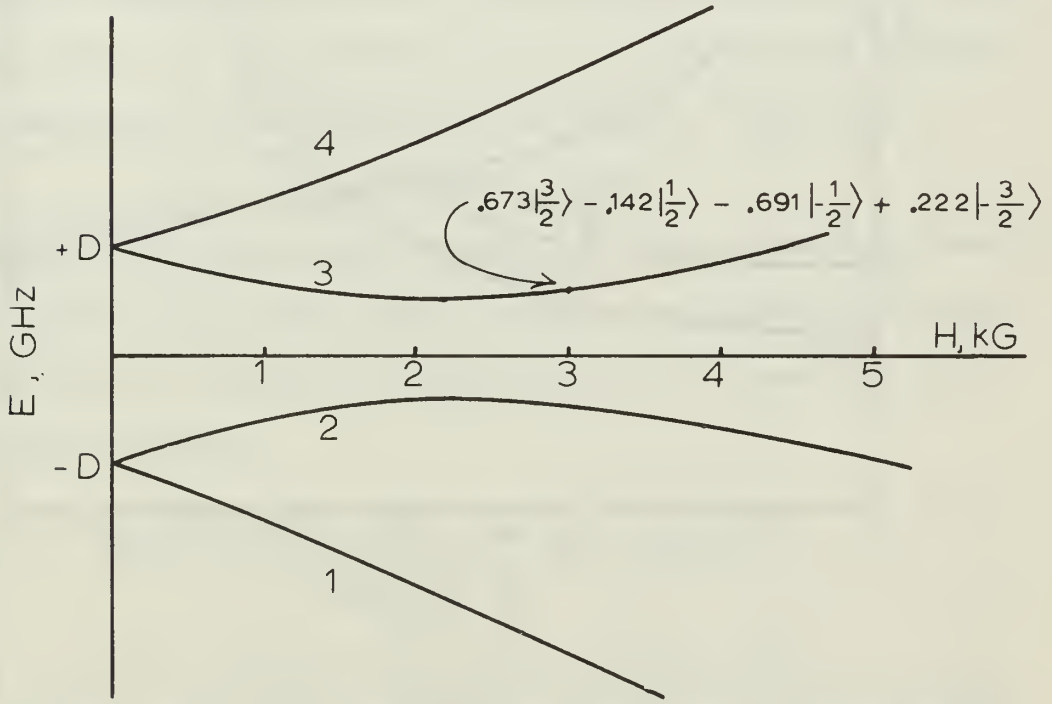

Fig. 3-3b. Energy levels of ruby for H at 50° to c-axis. State coefficients for level 3 at 3 kG are from Siegman.

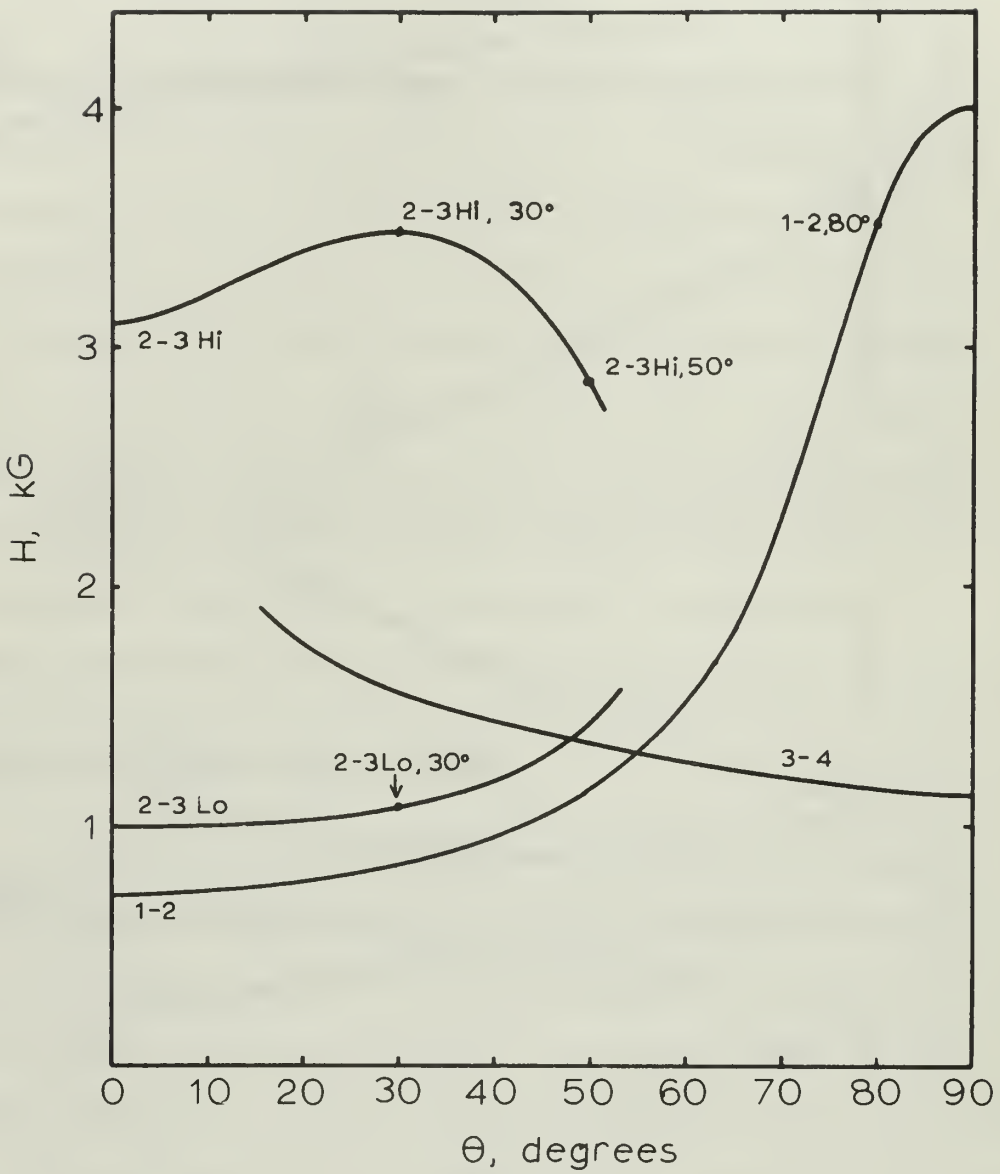

Fig. 3-4. Values of magnetic field H and magnetic field angle θ corresponding to transitions at 5.924 GHz. Transitions used in this experiment are shown.

Notice that we have also taken $g(E)$ over to $g(\nu)$; $g(\nu)$ is expected to be sharply peaked near the transition frequency $\nu = (E_b - E_a)/h$.

To proceed much further on the subject of transition probabilities at first seems rather pointless since our study is not really concerned with the strengths of the resonance lines. Later, however, we will apply our moment theory to the energy levels of ruby, and it will be necessary to construct matrix elements almost identical to those needed here. Also, if the technique for obtaining these matrix elements is developed now, we will be able to show some additional features of APR affecting the prosecution of our experiment. For this reason we continue.

Case I, Electron Paramagnetic Resonance (EPR)

For EPR, $\mathcal{H}_{int} = -\vec{\mu}\cdot\vec{H}_1$, where $\vec{\mu}$ is the magnetic dipole moment of the paramagnetic ion and $\vec{H}_1$ is the magnetic induction of the microwave field. In our experiment, $H_1 = H_1 \cos \omega t$ in the x-direction perpendicular to the ruby c-axis, and since $\mu_x = g\beta S_x$ then

$$\mathcal{H}_{int} = - g\beta H_1 S_x \cos \omega t$$

We next form matrix elements with $\mathcal{H}_{int}$. Since we are only interested in relative magnitudes between different transitions, we drop the constants and concentrate on expressions of the form $|\langle a|S_x|b\rangle|^2$. We take two levels

$$|a\rangle = a_1|\tfrac{3}{2}\rangle + a_2|\tfrac{1}{2}\rangle + a_3|-\tfrac{1}{2}\rangle + a_4|-\tfrac{3}{2}\rangle$$

$$|b\rangle = b_1|\tfrac{3}{2}\rangle + b_2|\tfrac{1}{2}\rangle + b_3|-\tfrac{1}{2}\rangle + b_4|-\tfrac{3}{2}\rangle$$

so that

$$\langle a|S_x|b\rangle = a_1b_1\langle\tfrac{3}{2}|S_x|\tfrac{3}{2}\rangle + a_2b_1\langle\tfrac{1}{2}|S_x|\tfrac{3}{2}\rangle + \cdots$$

$$+ a_2b_1\langle\tfrac{1}{2}|S_x|\tfrac{3}{2}\rangle + a_2b_2\langle\tfrac{1}{2}|S_x|\tfrac{1}{2}\rangle + \cdots$$

$$+ \text{remaining terms.}$$

The S_x matrix elements are found in any quantum mechanics book; in this particular case we get

$$\langle a|S_x|b\rangle = \frac{\sqrt{3}}{2}(a_1b_2 + a_2b_1 + a_3b_4 + a_4b_3) + (a_2b_3 + a_3b_2)$$

Using the values of a_i and b_i given by Siegman, this expression may be evaluated and squared, thereby giving the strength of the transition $|a\rangle \longrightarrow |b\rangle$. In general, we note that all transitions are possible at $\theta \neq 0^o$ where the states are mixed, but at $\theta = 0^o$ the selection rule $\Delta m = \pm 1$ holds and the transitions $\frac{3}{2} \longleftrightarrow \frac{1}{2}$, $\frac{1}{2} \longleftrightarrow \frac{3}{2}$, and $\frac{3}{2} \longleftrightarrow \frac{3}{2}$ are forbidden.

Case II, Acoustic Paramagnetic Resonance (APR)

The interaction Hamiltonian for APR has been developed by Altshuler, et. al.[6] for very general symmetries, and used to calculate the sound absorption coefficient σ. We write explicitly only the factors which contribute to lineshape:

$$\sigma = C\sum_{p=1}^{6} \alpha_p |\langle a|\mathcal{H}_p|b\rangle|^2 \, g(\nu)$$

where C is a constant, and α_p's are factors incorporating propagation and polarization direction of the acoustic wave relative to the crystal axes, and the $\mathcal{H}_p$'s are collections of spin operators. The most general form of this expression has been shown by Loudon[7] to be

$$\sigma = A[3S_z^2 - S(S+1)] + B(S_zS_+ + S_+S_z) + B^*(S_zS_- + S_-S_z)$$

$$+ CS_+^2 + C^* S_-^2$$

where A, B, C are constants and $S_\pm = S_x \pm i S_y$. This form has the following properties:

1) $\sigma = 0$ for $S = \frac{1}{2}$, therefore the expression only applies to the $S > \frac{1}{2}$ case.

2) The A terms have selection rule $\Delta m = 0$

3) The B terms have selection rule $\Delta m = \pm 1$

4) The C terms produce quadrupole interactions: $\Delta m = \pm 2$

Which of these terms appears in any specific case depends upon the polarization and direction of the acoustic wave. For the case of a longitudinal sound wave propagating down the c-axis of a trigonal crystal, this being our experimental situation, Altshuler's prescription yields

$$\sigma = C|\langle a|S(S+1) - 3S_z^2|b\rangle|^2 \, g(\nu)$$

where the constants have been absorbed into C. The angular dependence of this expression becomes evident when we calculate σ for our two mixed states $|a\rangle$ and $|b\rangle$ as before. The result is

$$\sigma = C|a_1b_1 + a_4b_4 - a_2b_2 - a_3b_3|^2 \, g(\nu)$$

For our purposes, the chief consequence of this calculation is that at $\theta \neq 0^\circ$, all transitions are possible, while at $\theta = 0^\circ$ all transitions are forbidden. The latter result is indeed unfortunate, for the theoretical expressions for moments would be materially simplified if we could perform our experiments on the unmixed states. We do, nevertheless, have the proper strengths for off-axis transitions.

So far, we have calculated the energy levels of ruby and have shown how to derive the transition probabilities of both EPR and APR resonances at any angle θ. Our final task is to evaluate, for ruby, the second moments of the transitions.

In the last section, we gave a general formula for the second moment of a system of levels, where the number of levels remained unspecified. In ruby, there are four levels so that R = 4; hence

$$\langle (h\Delta\nu)^2 \rangle = \frac{1}{4N} \sum_{ij}{}' \Big[|\langle 11|W_{ij}|11\rangle - \langle 21|W_{ij}|21\rangle - \langle 21|W|12\rangle|^2$$

$$+ |\langle 22|W_{ij}|22\rangle - \langle 12|W_{ij}|12\rangle - \langle 21|W_{ij}|12\rangle|^2$$

$$+ |\langle 13|W_{ij}|13\rangle - \langle 23|W_{ij}|23\rangle|^2 + |\langle 13|W_{ij}|31\rangle - \langle 23|W_{ij}|32\rangle|^2$$

$$+ |\langle 14|W_{ij}|14\rangle - \langle 24|W_{ij}|24\rangle|^2 + |\langle 14|W_{ij}|41\rangle - \langle 24|W_{ij}|42\rangle|^2 \Big]$$

We will use the convention that the levels which are participating in the transition are $|1\rangle$ and $|2\rangle$, while $|3\rangle$ and $|4\rangle$ are the other levels; since the formula is invariant with respect to interchange of $|1\rangle$ and $|2\rangle$ and also with respect to $|3\rangle$ and $|4\rangle$, there should be no further difficulty in sorting out the proper levels.

The form of W_{ij} is just that given by Van Vleck[2]:

$$W_{ij} = g^2\beta^2 \frac{[\vec{S}_i \cdot \vec{S}_j - 3(\hat{r}_{ij} \cdot \vec{S}_i)(\hat{r}_{ij} \cdot S_j)]}{r_{ij}^3} + \tilde{A}_{ij} \vec{S}_i \cdot \vec{S}_j$$

where r_{ij} is the distance between Cr^{3+} ions i and j, and $\hat{r}_{ij}$ is a unit vector in the $\vec{r}_{ij}$ direction. The first term is, of course, the well known interaction between two magnetic dipoles, and the last term represents an exchange coupling of magnitude $\tilde{A}_{ij}$. In

the last section, we also discussed the reasons for truncating W_{ij} to include only that part which commutes with the main Hamiltonian. This procedure amounts to throwing out all terms of W_{ij} which are non-diagonal in the W_{ij} matrix, and retaining only the diagonal terms. Expanding W_{ij} in spin variables and performing the truncation, we get

$$W_{ij} = \tilde{A}_{ij} \left[S_{zi} S_{zj} + \frac{1}{2} (S_{+i} S_{-j} + S_{-i} S_{+j}) \right]$$

$$+ B_{ij} \left[\frac{2}{3} S_{zi} S_{zj} - \frac{1}{6} (S_{+i} S_{-j} + S_{-i} S_{+j}) \right]$$

where

$$B_{ij} = 3g^2\beta^2 \left[\frac{\frac{3}{2} \gamma_{ij}^2 - \frac{1}{2}}{r_{ij}^3} \right]$$

and where γ_{ij} is the direction cosine between $\vec{r}_{ij}$ and the z-axis.

Since so many quantization conventions are in common usage for calculations such as the present one, we should, at this point, state explicitly which one we are employing. Our axes are fixed with respect to the crystal, with the z-axis in the direction of the crystal c-axis. We have chosen the quantization axis to be the z-axis, so that when the magnetic field is at some angle to this axis, the crystalline and magnetic field directions are "in competition" and the levels become linear combinations of the pure states (that occur when the magnetic field is along the z-axis). The direction cosine γ_{ij} occurring in the W_{ij} is always with respect to the quantization direction; therefore, it involves the angle between r_{ij} and the ruby trigonal axis. We thus see that sums such as ΣB_{ij} over all neighbors are independent of magnetic field direction

and, being constants of the experiment, can be calculated or measured once and for all.

The next step in obtaining the moments is to form the double matrix elements $\langle 12|W_{ij}|12\rangle$, $\langle 12|W_{ij}|21\rangle$,..., sum them, square the sums, and add the sums together, all according to the prescription given earlier. First, we put W_{ij} into the matrix element and obtain forms like, say, $\langle 12|S_{+i}S_{-j}|12\rangle$.

These are easily analyzed; for example:

$$\langle 12|S_{+i}S_{-j}|12\rangle = \langle 1|S_{+i}|1\rangle \langle 2|S_{-j}|2\rangle$$

$$= (a_1\langle\tfrac{3}{2}| + a_2\langle\tfrac{1}{2}| + a_3\langle-\tfrac{1}{2}| + a_4\langle-\tfrac{3}{2}|)S_+ (a_1|\tfrac{3}{2}\rangle + a_2|\tfrac{1}{2}\rangle + a_3|-\tfrac{1}{2}\rangle + a_4|-\tfrac{3}{2}\rangle$$

$$X(b_1\langle\tfrac{3}{2}| + b_2\langle\tfrac{1}{2}| + b_3\langle-\tfrac{1}{2}| + b_4\langle-\tfrac{3}{2}|)S_- (b_1|\tfrac{3}{2}\rangle + b_2|\tfrac{1}{2}\rangle + b_3|-\tfrac{1}{2}\rangle + b_4|-\tfrac{3}{2}\rangle$$

$$= (a_1^2\langle\tfrac{3}{2}|S_+|\tfrac{3}{2}\rangle + a_1a_2\langle\tfrac{3}{2}|S_+|\tfrac{1}{2}\rangle + \ldots\ )(X(b_1^2\langle\tfrac{3}{2}|S_-|\tfrac{3}{2}\rangle + b_1b_2\langle\tfrac{3}{2}|S_-|\tfrac{1}{2}\rangle + \ldots)$$

$$= [\ 3\ (a_1a_2 + a_3a_4) + 2a_2a_3][\ 3\ (b_2b_1 + b_4b_3) + 2b_3b_2]$$

The a's and b's are now looked up in Siegman for the proper magnetic field strength and angle, and the matrix element evaluated numerically. Double matrix elements can then be formed from the other components of W_{ij} in like fashion and the complete moment expression readily evaluated. The outcome is of the form

$$h^2\langle\Delta\nu^2\rangle = \frac{1}{4N}\ \sum_{ij}{}' [\alpha\widetilde{A}_{ij}^{\,2} + \beta\widetilde{A}_{ij}\,B_{ij} + \delta\ B_{ij}^{\,2}]$$

where α, β, and δ result from our matrix element calculations.

In order to calculate the summation over pairs, we must remember and incorporate the fact that ruby is a dilute crystal and that only a few of the neighboring Al sites of a given Cr ion are occupied by

other Cr ions. Kittel and Abrahams[10] have shown that $\sum'_{jk}$ should first run over the j occupied sites, giving $\sum'_{jk} = N\sum_k$, where k indicates all actual Cr neighbours of an occupied site. But this sum is the same as saying that the contribution from every site, occupied or unoccupied, is just the contribution from that site if it were occupied times the occupation probability f, so that

$$\sum'_{jk} = N \sum_k = Nf \sum_k$$

all pairs — all occupied neighbor sites — all possible neighbor sites

This gives us our final moment

$$h^2\langle\Delta\nu^2\rangle = \frac{f}{4}\left(\alpha \sum_k \tilde{A}_k^2 + \beta \sum_k \tilde{A}_k B_k + \delta \sum_k B_k^2\right)$$

or

$$\boxed{\langle\Delta\nu^2\rangle = \frac{f}{4}\left(\alpha \sum_k \tilde{A}_k^2 + \beta \sum_k \tilde{A}_k B_k + \delta \sum_k B_k^2\right)}$$

if we divide $\tilde{A}$ and B by h and express all energies in units of frequency.

Several conclusion can now be drawn concerning the second moment.

1. As we noticed in the last section, the transition inducing interaction does not appear in our expression and therefore the second moment should be the same for APR as for EPR.
2. The second moment is directly proportional to the concentration of the magnetic impurity.
3. There is an angular dependence in $\langle\Delta\nu^2\rangle$ brought about by the dependence of α, β, and δ on the amount of state mixing at different angles. If we know the sums in $\tilde{A}_k$ and B_k (which are essentially constants) we can then predict the moment at any angle.
4. Contrary to the results of Loudon[7], we see that for levels with crystal field splitting, the exchange does contribute to $\langle\Delta\nu^2\rangle$, both in a squared term and in a cross term with B_k. This is a

highly favorable result because it removes the necessity for measuring the fourth moment in order to get exchange information. It turns out that fourth moments, which receive their main contributions from the wings of the absorption curve where the signal to noise ratio is low, are extremely difficult to measure.

We now have a choice as regards applying the second moment expression to our experimental results. Since α, β, and δ can be calculated from matrix elements, and since f is just the known Cr concentration of our samples, we could treat the expression as an equation in three unknowns: $\Sigma\, \tilde{A}_k^{\,2}$, $\Sigma\, \tilde{A}_k B_k$, and $\Sigma\, B_k^{\,2}$. By measuring three moments with different α, β and δ coefficients, we could then solve the three corresponding equations for each sum. On the other hand, since the form of B_k is well known, we could calculate $\Sigma\, B_k^{\,2}$ from a knowledge of the Al_2O_3 crystal structure and be left with only the remaining two sums, $\Sigma\, \tilde{A}_k^{\,2}$ and $\Sigma\, \tilde{A}_k B_k$, as unknowns. We have chosen the latter alternative -- especially since the summation part of $\Sigma\, B_k^{\,2}$ has already been performed in a nuclear magnetic resonance study by Verber, Mahon, and Tantilla[19].

$$B_k = -3g^2\beta^2 \frac{(\frac{3}{2}\gamma_k^{\,2} - \frac{1}{2})}{r_k^{\,3}}$$

so that, dividing by h and squaring,

$$\Sigma\, B_k^{\,2} = \frac{9}{4} \frac{g^4\beta^4}{h^2} \left[\sum_k \frac{(3\gamma_k^{\,2} - 1)}{r_k^{\,6}} \right] \text{in } H_z^{\,2}$$

where the summation is to be taken over all possible nearest neighbor sites. Verber, et al. quote a value of $.0176A^{-6}$ for the geometric factor in brackets; using g = 2.00, we thus arrive at the figure of $\Sigma\, B_k^{\,2} = 107$ GHz^2. Hence,

$$\langle \Delta\nu^2 \rangle = \frac{f}{4} [\alpha \Sigma \tilde{A}_k^2 + \beta \sum_k \tilde{A}_k B_k + \delta (107 \text{ GHz}^2)]$$

Without an explicit knowledge of the exchange $\tilde{A}_k$, we cannot proceed any further theoretically.

By way of motivation for the present experiment, we should mention that the above formula has been used by Ishiguro, Kambe, and Usui[4] in a study of the second moments of Ni^{++} in nickel fluosilicate. By taking angles of $\theta = 0^\circ$ and 90°, they showed that $\beta = 0$ and the cross term $\Sigma \tilde{A}_k B_k$ does not appear. They then calculated ΣB_k^2 for their crystal and solved for the exchange term $\Sigma \tilde{A}_k^2$. Assuming that $\Sigma \tilde{A}_k^2$ was due to the six nearest neighbors only, then $\Sigma \tilde{A}_k^2 = 6\tilde{A}^2$ and they were able to find $\tilde{A}^2$. Because they lacked the cross term, they were not able to determine the sign of $\tilde{A}$, but they were highly successful in determining its magnitude.

If we could achieve acoustic resonance in ruby at 0°, it turns out that our cross term would also vanish, and we could solve for $\Sigma \tilde{A}_k^2$ only. But the transition probability for this angle is, as we have shown earlier, zero, thereby forcing us to higher angles where we must use the full moment expression. We do have, however, an opportunity to determine the sign of the exchange.

In our experiment, we have chosen four transitions (see Fig. 3-4) to measure as a function of Cr concentration: 2-3 Hi at 50°, 2-3 Hi at 30°, 2-3 Lo at 30°, and 1-2 at 80°. Using the state coefficients from Siegman, we have calculated α, β and δ by CDC 1604 computer for each transition; the results are listed in Table 3-1. APR and EPR lineshapes of these transitions were then taken for six rubies of Cr concentration .005%, .02%, .05%, .1%, .3%, and 1% by weight. No attempt was made to

systematically study angular dependence.

This completes our application of the theory to the ruby crystal. In Chapter VI, when we examine the experimental results, we will return to the ideas of this section and attempt to estimate the second moment by using the somewhat meager data on $\tilde{A}_{ij}$. First, however, we will discuss the experiment itself.

transition	α	β	δ
2-3 Hi, 50^{o}	9.475	-2.453	1.373
2-3 Hi, 30^{o}	5.925	.971	1.373
2-3 Lo, 30^{o}	15.291	18.019	7.539
1-2, 80^{o}	7.232	-.218	.935

Table 3-1. Coefficients of the second moment equation

$$\langle \Delta\nu^2 \rangle = \frac{f}{4} (\alpha \Sigma\tilde{A}_k^2 + \beta\Sigma\tilde{A}_k B_k + \delta\Sigma B_k^2)$$

for four transitions.

CHAPTER IV

THE ACOUSTIC PARAMAGNETIC RESONANCE EXPERIMENT

In this section we will discuss the acoustic paramagnetic resonance experiment. In Section 1, we will describe our ruby crystals and the bonding of transducers. In Section 2, we discuss the microwave equipment, followed by the signal detection scheme in Section 3. Finally, we show how to get the second moments in Section 4, and we discuss their accuracy.

1. Crystals and Bonding

The ruby crystals used in this experiment were purchased from Union Carbide Corporation, Linde Division, and Adolph Meller Company. All crystals were cylindrical, ¼" in diameter by 1 1/8" long, having frosted walls, and ends precision ground to a parallelism of 2 arc seconds and a flatness of 1/20 wavelength of sodium light. The original boules were grown by the flame fusion process. Although the rods were specified to have their crystal c-axis parallel to the rod axis, we took x-ray patterns and discovered a slight misorientation. Table 4-1 summarizes this information.

Sample	Concentration	c-axis Misalignment	Manufacturer
1	.005%	4.5°	Adolph Meller
2	.02	2	Linde
3	.05	0	Linde
4	.10	1.5	Adolph Meller
5	.3	4.5	Linde
6	1.0	3	Linde

Table 4-1. Data on ruby samples

All crystals were of standard quality except for rubies 2 and 5, which were Linde Superior Internal Quality for better crystalline uniformity.

In order to propagate sound pulses through ruby, it is necessary to provide a transducing material. We first attempted unsuccessfully to bond ¼" diameter by ¼" long x-cut quartz crystals to the rubies using indium as a bonding material as described by Weeks[9]. It was, however, difficult to control the rather critical bonding temperatures with this technique; consequently, our bonds turned out either too thick or prohibitively nonuniform and we abandoned the method.

In our next attempt, we tried various organic oils and greases as bonding agents, again using our ¼" long quartz transducers. The bonds were aligned at room temperature in a 500 MHz test apparatus (to be described later), but this technique was also unsuccessful. The long quartz transducers have two disadvantages: first, they have a low Q and hence a low conversion efficiency; secondly, a bond echo is produced when the sound wave passes through the bond, thereby wasting energy and often obscuring the real echo from the ruby.

In the final bonding procedure, we used resonant quartz wafers instead of the longer quartz transducers. The transducers, purchased from Valpey Corporation, were x-cut with a 91 $\pm$ 2 MHz resonant frequency and 7/32" in diameter. The thickness corresponding to this frequency is about 1.5 mil; in order to guarantee good performance at high harmonics, the faces were polished to .00001" parallelism and 1/20 wavelength (of sodium light) flatness. These crystals are highly resonant, even at 6 GHz, and the conversion efficiency is much higher than with the larger transducers. Also, there is no bond echo.

We give a step-by-step description of the crystal bonding process in the Appendix; suffice it to say here that the bonding agent is Nonaq Stopcock Grease (Fisher Scientific Co.) and that the transducers can be successfully fixed to the end of the ruby. Fig. 4-1 shows a completed bond.

After making the bond, it was checked out on a 500 MHz pulser-receiver setup to see if it was good. The checkout apparatus was very simple: a 1 watt General Radio 1209 BL unit oscillator, receiving trigger pulses from a Teletronix PG-200AA pulse generator, fed 500 MHz, 1 μsec pulses directly to a Navy AN/APR-4Y receiver. An adjustable frequency reentrant cavity[20] and a tuning stub were then coupled in by tee fittings. After inserting the quartz-ruby bond into the test cavity, the resulting receiver echoes could be directly observed on an oscilloscope. Over 100 observable echoes resulted, depending upon the bond quality; therefore, poor bonds could be quickly detected and redone. Typicable bonds, as could be seen by observing interference fringes, had a thickness of a few wavelengths of light, but the bond thickness was not particularly uniform. This fact did not seem to affect the high frequency echo-train too much; indeed, the lack of rigidity of the thin transducer may have helped the bond to remain intact at low temperatures.

2. The Microwave Equipment

A diagram of the J band hypersonic spectrometer is shown in Fig. 4-2. A Teletronix PG-200AA pulse generator provided 1 μsec, 100 V pulses at a repetition rate of 103 Hz to a modulator from a Navy SU radar. The modulator then drove a watercooled Litton L-3467 magnetron, which in turn produced 5.924 GHz pulses of 1.8 kw peak power. An

Figure 4-1. Ruby sample with bonded transducer on upper end and reentrant cavity. Microwave coupling loop screws into top of cavity.

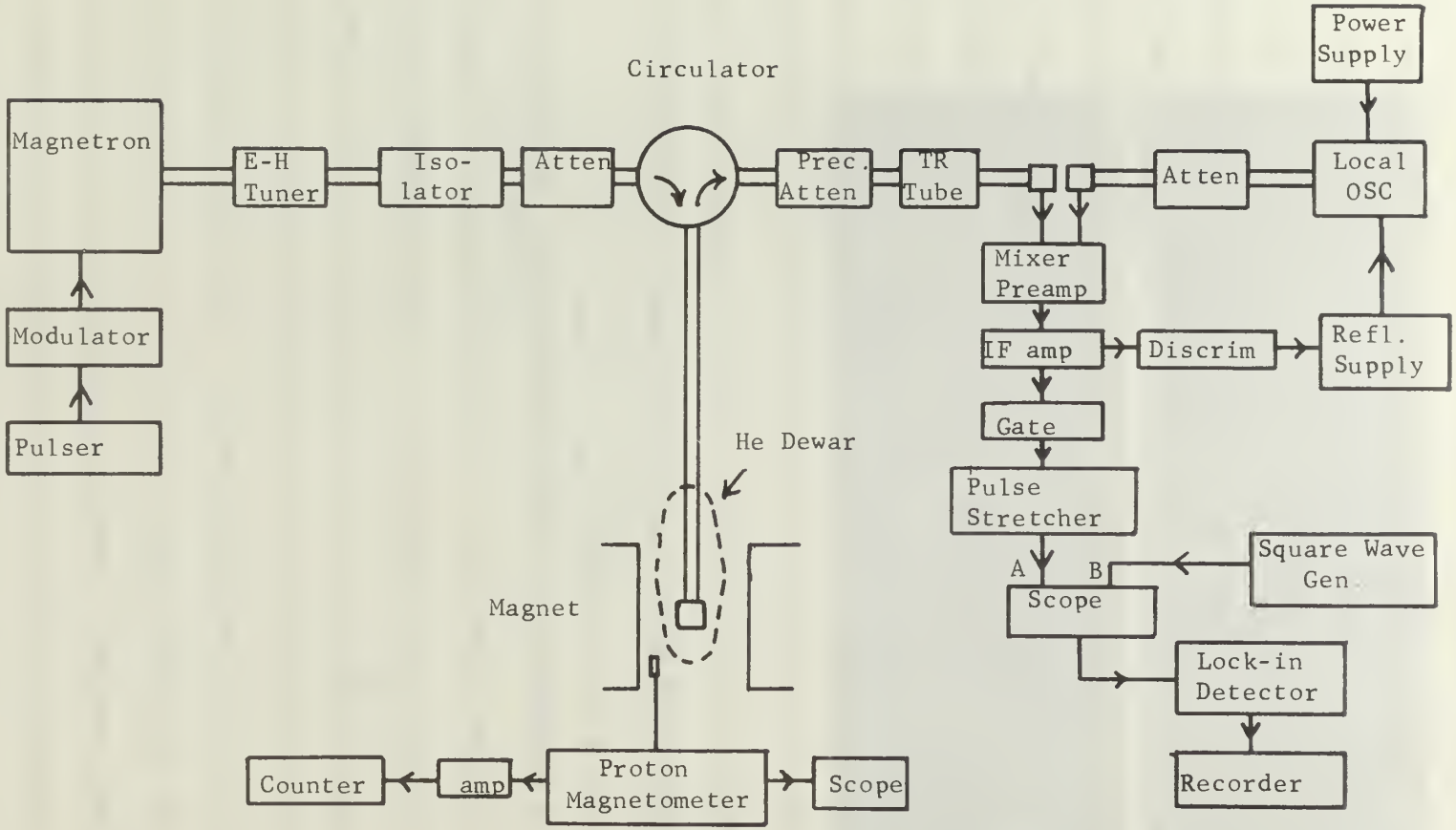

Fig. 4-2. The hypersonics spectrometer

attenuator was used to reduce the power during the experiment to 100 watt or less, depending upon the quality of the bond. In order to reduce heat leakage into the helium bath, the signal was coupled from the waveguide into a copper plated, thin wall, stainless steel, coaxial waveguide, to which the sample cavity was attached.

The cavity was of the reentrant type (Fig. 4-1) with internal dimensions of 1.63 cm diameter by .712 cm depth. A raised post of height 1.25 mm served to direct the electric field into the transducer. The microwave power was coupled into the cavity by a small loop oriented with its plane perpendicular to the cavity magnetic field. In order to adjust the resonant frequency of the cavity to a transducer harmonic, the ruby was mounted in a collar; the position of the collar and, hence, the depth of the ruby in the cavity could be controlled while the cavity was immersed in liquid helium. Prior to the experiment, but after cooldown, the ruby position was easily adjusted for maximum echo height. The cavity Q was about 400.

The received echoes were passed through a TR (transmit-receive) tube, which provided a dead short to the main pulse and protected the receiver, to an LEL CAC-2 mixer-preamplifier. A Varian X-26E klystron provided a beat signal 30 MHz away from the main frequency. The 30 MHz difference signal was then amplified by an LEL 3378 IF amplifier which put out the rf signal and the detected envelope. The 30 MHz rf signal was used for local oscillator control; it was fed to an LEL 3379 discriminator which then provided a correction voltage for the reference klystron. The detected signal from the IF amplifier was then available for oscilloscope observation or, as we shall describe in the next section, for signal processing. Figure 4-3 shows a typical echo train, first when

(a)

(b)

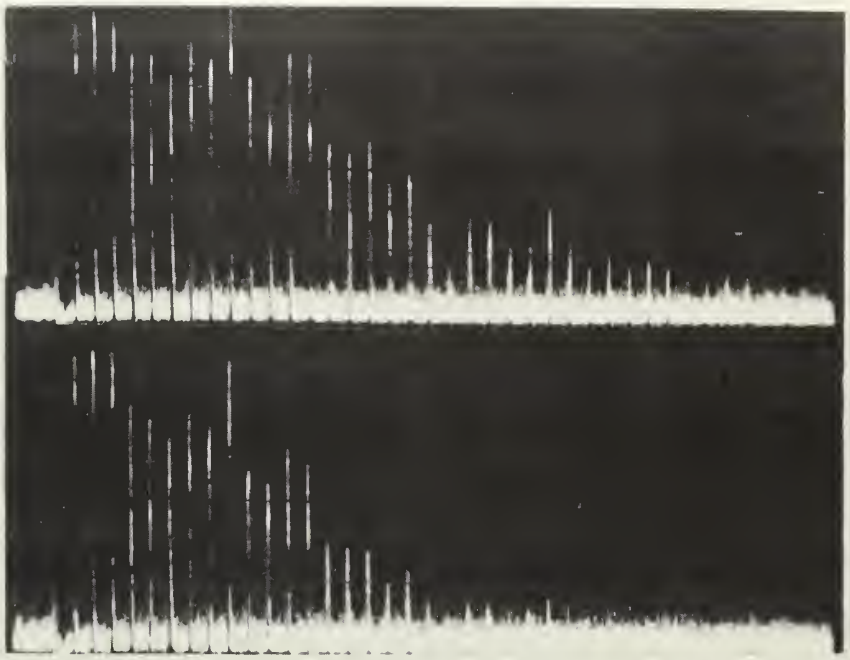

Fig. 4-3. Acoustic echoes from ruby sample.
a) Off resonance condition.
b) On resonance condition.
Scale is .5v/cm vertically, 20 μsec/cm horizontally.

the magnetic field is off resonance, and then when it is on resonance.

3. Pulse Detection and Calibration

In order to monitor the resonance, the echo train was passed through a gate which selected one pulse for observation. Since the duty cycle of this pulse was so low (10^{-4}) it was necessary to stretch the pulse out; this was done very simply by passing it through a diode to a large grounded capacitor. The capacitor had a rapid charging time (< 1 μsec) due to the low forward resistance of the diode and a long discharge time determined by the backward resistance of the diode and/or the input impedance of the instrument detecting the capacitor's charge. In this way, the pulse was converted from a 1 μsec spike to an exponential decay with decay time $\tau \simeq 5$ msec. This signal was then added to a positive going 103 Hz square wave such that the signal appeared during the first half of the repetition period and the square wave appeared during the second half (when the exponential tail of the signal was small). The square wave thus served as a comparison for the signal, converting it to an AC signal whose average value off resonance was zero. Detection of this signal was then effected by an EMC model RJB phase sensitive amplifier, the output of which provided a DC voltage for a Varian G-10 strip chart recorder. Synchronization signals for the modulator pulser, gate pulser, square wave generator and phase sensitive detector were supplied by a Hewlett Packard 200 AB sine wave generator.

The magnetic field was provided by a Varian V-4012-3B 12" magnet operated from a V-2100A power supply and controlled by a Varian V-FR2100 Fieldial control unit. Uniformity of the field was better than .05 G over the sample, and the Fieldial control unit gave extremely good stability in time. Calibration of the field was obtained by using an

Alpha AL67 NMR gaussmeter, modified so that the NMR frequency could be extracted, amplified, and read on a Beckman 6127 frequency counter. Since the NMR frequency was stable to $\simeq$ .01 KHz, the accuracy was about one part in 10^6 for a 10 MHz NMR voltage.

Since quartz transducers are highly absorptive to high frequency sound at high temperature, the experiment was performed in liquid helium. The low temperature apparatus was of the standard type: an outer dewar filled with liquid nitrogen surrounded an inner dewar filled with liquid helium. The vacuum jacket on the inner dewar was connected to a small forepump only; when liquid helium was introduced this jacket was sealed off and allowed to cryopump. Control of the inner jacket vacuum turns out to be essential in order to achieve slow cooldown times and prevent breaking of the transducer bond.

In order to reduce bubbling in the cavity, the helium was pumped below the λ-point. The temperature at which all lines were measured was $1.7^{o}K$.

A typical APR lineshape was calibrated as follows. The magnetometer was set to some field value, then, when the magnetic field swept through the magnetometer resonance, a pen mark was put on the chart paper and the frequency was read. The magnetometer was then reset and the process repeated, providing for about six or seven marks per chart. The frequencies were then converted to magnetic field values and plotted against chart distance; in all cases, the relationship was linear. The accuracy of this procedure was limited maily by the rate at which the magnetometer signal crossed the oscilloscope face; accuracy is generally $\pm$ .5 gauss and in no case worse than $\pm$ 1 gauss.

Immediately upon completion of a chart trace, a signal calibration was made by setting in known amounts of attenuation with the precision attenuator and recording the corresponding recorder pen positions. This procedure accounted for all non-linearities introduced between the attenuator and the recorder--virtually the whole detection system. A calibration curve of dB attenuation versus pen position was then made and the chart ordinates corrected to read dB. The accuracy here depended upon the amount of background noise, but generally can be set at $\pm$ 5%. It was necessary to avoid sweeping the resonance too fast on some resonances, since the trace can be controlled by the lock-in amplifier integration time rather than the signal itself. This effect was calculated beforehand and a set of maximum allowable chart slopes was obtained and never exceeded in the experiment.

The overall sensitivity was a few tenths of a decible, however on the lowest concentration ruby (.005%) no signal was detectable. Figure 4-4 shows two sample curves, one very good and the other rather poor. These graphs represent the extremes of our data.

4. Data Evaluation

Once the data was taken, the next step was to obtain the second moments. Each chart was first digitized to between 40 and 80 points and then analyzed by IBM 360 computer. The computer program performed the following calculations:

1. For a given transition, five values of the energy level separation ν corresponding to various magnetic fields H were entered. For example, in the transition 2-3 Hi at 50° which occurs at H = 3000G, ν was entered for H = 2000G, 2500G, 3000G, 3500G, and 4000G. The program then fit these pairs

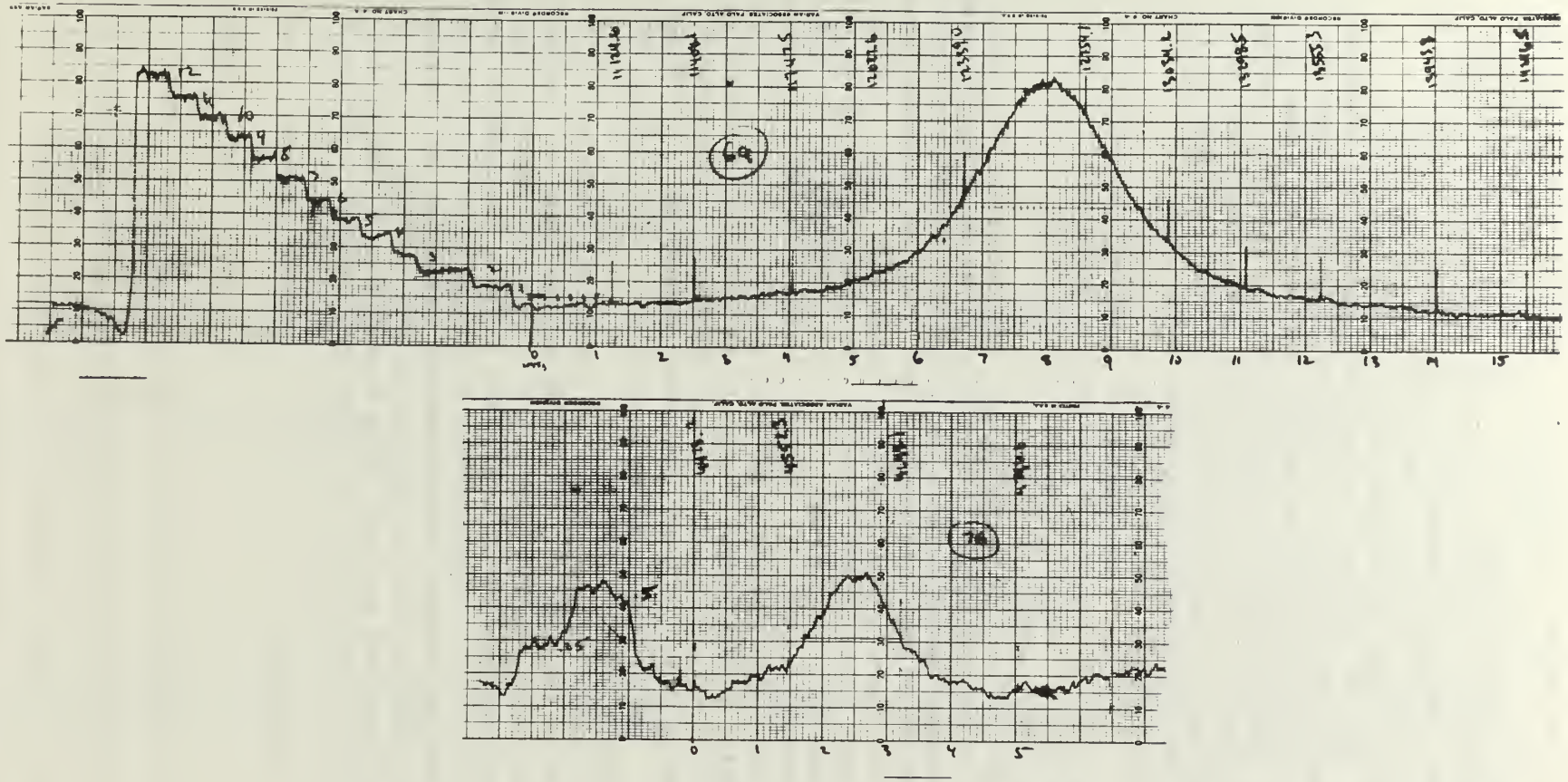

Fig. 4-4. Two sample APR charts. Upper chart is 2-3 Hi at 50^{o}, 1% Cr concentration. Lower chart is 2-3 Lo at 30^{o}, .02% Cr concentration. Steps on left of chart calibrate vertical axis in dB; numbers on top of chart are NMR proton resonance frequencies for magnetic field calibration.

with a five degree polynomial and generated a frequency point for each digitized value of H. This process converts the magnetic fields to frequencies, automatically accounting for asymmetry caused by nonlinearities in the ν-H curve.

2. The area of the line was calculated using trapezoidal increments. Each ordinate was then divided by the area, thereby normalizing the line and yielding the true lineshape $g(\nu)$.
3. The second moment was calculated.
4. Values of H, ν, and $g(\nu)$ were read out along with the value of the second moment.

It must be remembered that the moment calculation is highly sensitive to the behavior of the line's wings, yet it is in the wings where the signal to noise ratio is the poorest. The limiting factor on our experimental accuracy is just this effect, rather than the approximations inherent in digital integration. We therefore feel that our moments have an accuracy ranging from $\pm$ 10% for the strong lines, up to $\pm$ 50% for weak, and consequently noisy, lines.

In addition to the moments, the widths of the lines at the half-power points were obtained by interpolating between the computer printout values. These half-widths were dependent mainly on the frequency calibration and therefore are felt to be accurate to a few percent.

CHAPTER V

THE ELECTRON PARAMAGNETIC RESONANCE EXPERIMENT

Of the equipment described for the APR experiment, only the crystals and DC magnet system are the same for EPR. The microwave equipment and detection system for EPR are different, as we will describe in the first part of this chapter. The second part will be devoted to the data analysis and experimental accuracy.

1. Microwave Equipment and Detection

The J band microwave spectrometer used in this experiment is of standard superheterodyne design as shown in Fig. 5-1. Both signal and local oscillators were Varian X-26E klystrons operated in the CW mode at 5.924 GHz. The signal was first fed through an E-H tuner, isolator and two 20 dB attenuators to a hybrid tee. Although the hybrid tee was initially set up to work as a microwave bridge, this proved to be unnecessary in the experiment, with the result that 50 dB of attenuation was permanently introduced into the reference arm.

The signal side of the hybrid tee was connected first to a frequency meter, then to a directional coupler, and finally to the cavity. Having the frequency meter in the cavity arm allowed us to lock on to the meter resonance if necessary, but this option was never used. The directional coupler was useful for tuning the klystron to the cavity and measuring the frequency, neither of which measurements required the receiver.

The cavity was a section of J-band waveguide 7.18 cm long operating in the TE_{102} mode. The ruby was inserted through the shortest dimensions of the cavity midway between the aperture and the cavity end; the transverse magnetic field was therefore perpendicular to the ruby c-axis. A

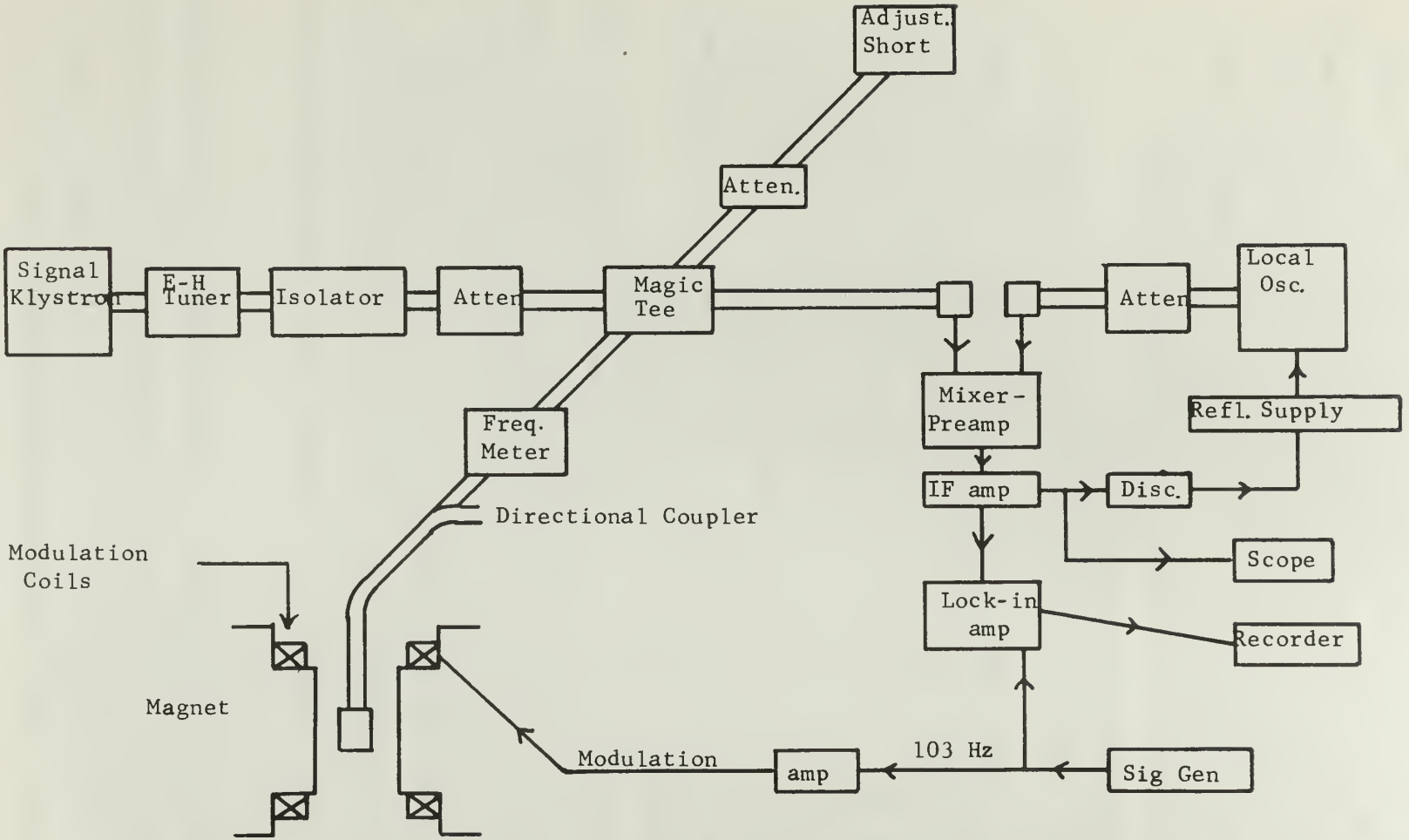

Fig. 5-1. The EPR spectrometer. Automatic frequency control not shown.

small metal or plastic screw could be inserted in the cavity bottom for fine tuning; coarse tuning was effected by changing the aperture size, normally set near, but not on, critical coupling. Cavity Q's were about 3000 with the ruby in place.

The return signal from the cavity was sent directly to an LEL CAC-2 mixer-preamplifier and the derived 30 MHz difference signal amplified in an LEL 3378 IF amplifier. The rf output from the amplifier was used two ways: first, it was monitored on an oscilloscope so that its change during resonance absorption could be checked; secondly, it was fed to an LEL 32B93 discriminator (modified for CW operation), the output of which was used as a correction voltage to lock the reference oscillator to the signal. A detected rf envelope, also provided by the IF amplifier, was fed directly to an EMC model RJB lock-in amplifier, the DC output of which then drove a Honeywell Electronik 19 recorder.

One feature of the spectrometer is not shown in Fig. 5-1. In order to protect against frequency drift and, more critically in a lineshape measurement, to guarantee that only the absorptive part of the complex susceptibility was observed, the signal klystron was locked onto the cavity resonance. To do this, the signal klystron reflector voltage was modulated at 10 kHz by an external sine wave generator. Due to the cavity characteristic, the received signal exhibited this modulation as an amplitude modulation, with the following properties: If the klystron frequency was situated on one side of the cavity, an approximate sine wave resulted; if the frequency lay on the other side, a sine wave with the opposite phase appeared; if the frequency coincided with the cavity center frequency, only a small second harmonic appeared. The sine wave was then phase sensitively detected and the resulting error

voltage added to the signal klystron reflector such that the signal frequency followed the cavity while the cavity shifted during passage through the line. A considerable reduction in the signal to noise ratio also resulted, indicating a lack of frequency stability without the automatic frequency control (AFC) feature.

The static magnetic field was provided by the same system used in the APR experiment. This field was modulated, however, by passing a sinusoidal current through coils wrapped about the magnet pole faces. The modulation frequency was 103 Hz, a frequency which is easily separable from the 10 kHz AFC signal but slow enough to accommodate the long relaxation time of ruby. The effect of the modulation was to cause the cavity reflection to oscillate correspondingly as determined by the shape of the ruby absorption characteristic. Since it was only the 103 Hz component of the cavity reflection that was ultimately seen by the lock-in amplifier, the resulting chart was the derivative of the true absorption line. In order to avoid distortion of the line, the amplitude of the modulating field was never more than 3G peak-to-peak.

The low temperature apparatus was not used for the EPR experiment since the lines could be easily observed at room temperature.

Most of the curves were obtained with about 10 μW of power to the cavity, although this value was raised to as much as 100 μW in some instances. Several curves exhibited consistent anomalies in their lineshapes, perhaps due to some paramagnetic impurity in the crystal. These were largely unexplainable; in any case, data from these curves was omitted in the final results. A typical derivative trace is shown in Fig. 5-2.

We now discuss several points relative to obtaining good EPR data.

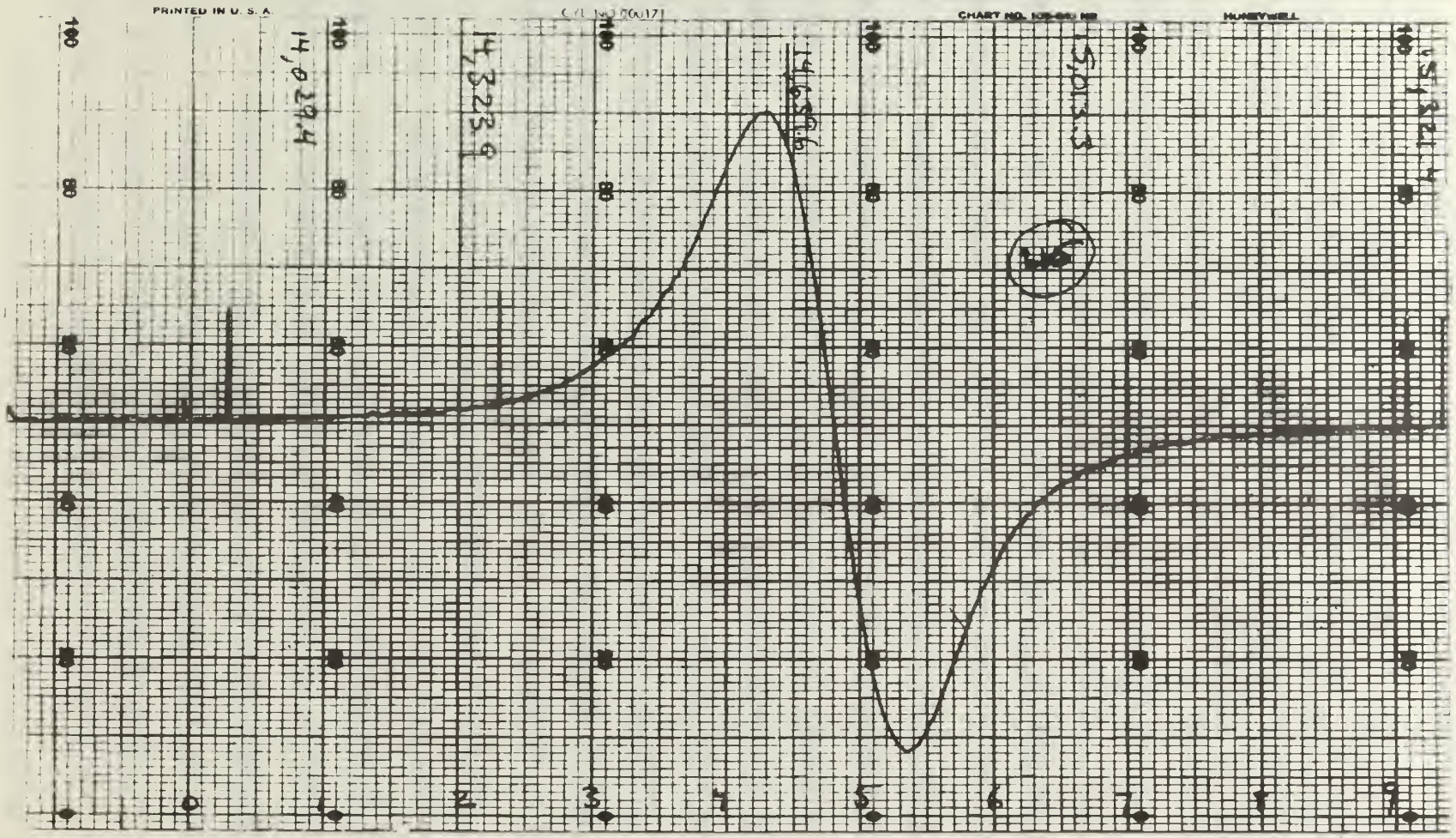

Fig. 5-2. Sample EPR derivative trace. Numbers at top are NMR proton resonance frequencies for magnetic field calibration.

In order to observe the true lineshape of an EPR transition, it is necessary to measure only the power absorption of the sample, but this quantity is not, in general, simply related to the cavity reflection. If E_{in} and E_{out} are the signals into and away from the cavity, R is the on-resonance effective cavity resistance, and Z_o is the characteristic impedance of the waveguide, then

$$\frac{E_{out}}{E_{in}} = \frac{R - Z_o}{R + Z_o}$$

and we see that E_{out} does not vary linearly with R. The resolution of this problem has been discussed thoroughly by Feher[21]; he has shown that in the limit of small (ideally, differential) changes in the cavity Q during resonance, the change in E_{out}, ΔE_{out}, is proportional to the true lineshape. We have assessed the errors involved in this technique with the following result: if E_{out} changes by 1% during the resonance, then the error in the true lineshape is also 1%. For this reason, the full rf envelope from the receiver was observed during every run. If the height of the envelope changed by more than $\approx$ 1%, the cavity Q was lowered by changing the cavity iris size, and this lessened the change in E_{out} due to the ruby resonance.

Another difficulty that occurs in EPR is the fact that the data appears in derivative form. In order to obtain the moments, one must first integrate the derivative to obtain the absorption curve, then integrate again in order to finally obtain the area and moments. The effect of the first integration on the moments can be very critical, for if the two lobes of the derivative curve differ in area by only a few percent, the absorption curve will not return exactly to the baseline

in one of its wings, and it is mostly the shape of the wings that determines the size of the moment.

In our experiment, it turned out to be very difficult to match the lobe sizes of the derivative curves to better than a few percent; for this reason, it was not possible to get moments. We feel that with more time and considerable effort, the accuracy of the raw data could have been adequately improved; however, in light of the fact that the APR moments resisted quantitative interpretation anyway, we restricted our results to EPR linewidths, for which the present data was sufficient.

2. Data Analysis

The analysis of the EPR data was identical to the APR analysis except in the initial conversion of the line to an absorption line. Values of H were derived from gaussmeter frequency markers on the chart and plotted against chart inches. The resulting calibration curve was linear in every case, yielding magnetic field values for each point on the chart trace. The chart was then digitized to between 50 and 100 points and analyzed by IBM 360 computer. The computer program performed the following functions:

1. The derivative trace was integrated using trapezoidal increments and magnetic field abscissas.
2. The magnetic field was converted to frequency values ν, in exactly the same way as in the APR analysis.
3. The area of the absorption curve was calculated and used to normalize the absorption line ordinates so that the area was unity. The ordinates thus became values of $g(\nu)$.
4. Moments were calculated.
5. The program printed out $g(\nu)$ versus ν and H for each digitized point.

Half-widths, corresponding to the full width at half power, were obtained by interpolating between the computer print out values. The half-widths are thus felt to be accurate to within a few percent.

CHAPTER VI

RESULTS AND DISCUSSION

In this section, we will present the measured second moments for APR and relate them to theory. Near the end of the section, we will also display EPR and APR half-widths and discuss them qualitatively.

The second moments of our four transitions are plotted in Fig. 6-1 as a function of Cr concentration. We note several features of these curves:

1. At 1% concentration, the curves have widely different moments, varying from .007 GHz^2 to .073 GHz^2.
2. The curves approach a constant value of the order of 10^{-3} GHz^2 as the concentration is lowered below about .05%. The effect is independent of the transition.
3. From the standpoint of our theory, the most important result is the extreme smallness of the measured moments. Using only the dipolar interaction, the second moment is predicted to be $\langle \Delta\nu^2 \rangle \sim$ (concentration) $(\Sigma B_k^2) \sim (1\%)(107\ GHz^2) \sim 1\ GHz^2$ for a 1% Cr concentration ruby. But as experimentally measured, the largest moment at 1% is $\approx .07\ GH_z^2$.

We begin our discussion of the data with an explanation of the moment size.

The fact that measured ruby second moments might be smaller than theory predicts has been alluded to by Manenkov and Fedorov[22], and Grant and Strandberg[23], although neither of these authors actually measured the moments. Manenkov and Fedorov measured EPR line widths ϵ at $\theta = 0^\circ$ and assumed either a Gaussian line, where $\langle \Delta\nu^2 \rangle = .171\epsilon^2$, or a Lorentzian line with cutoff at 5ϵ (a Lorentzian lineshape must be

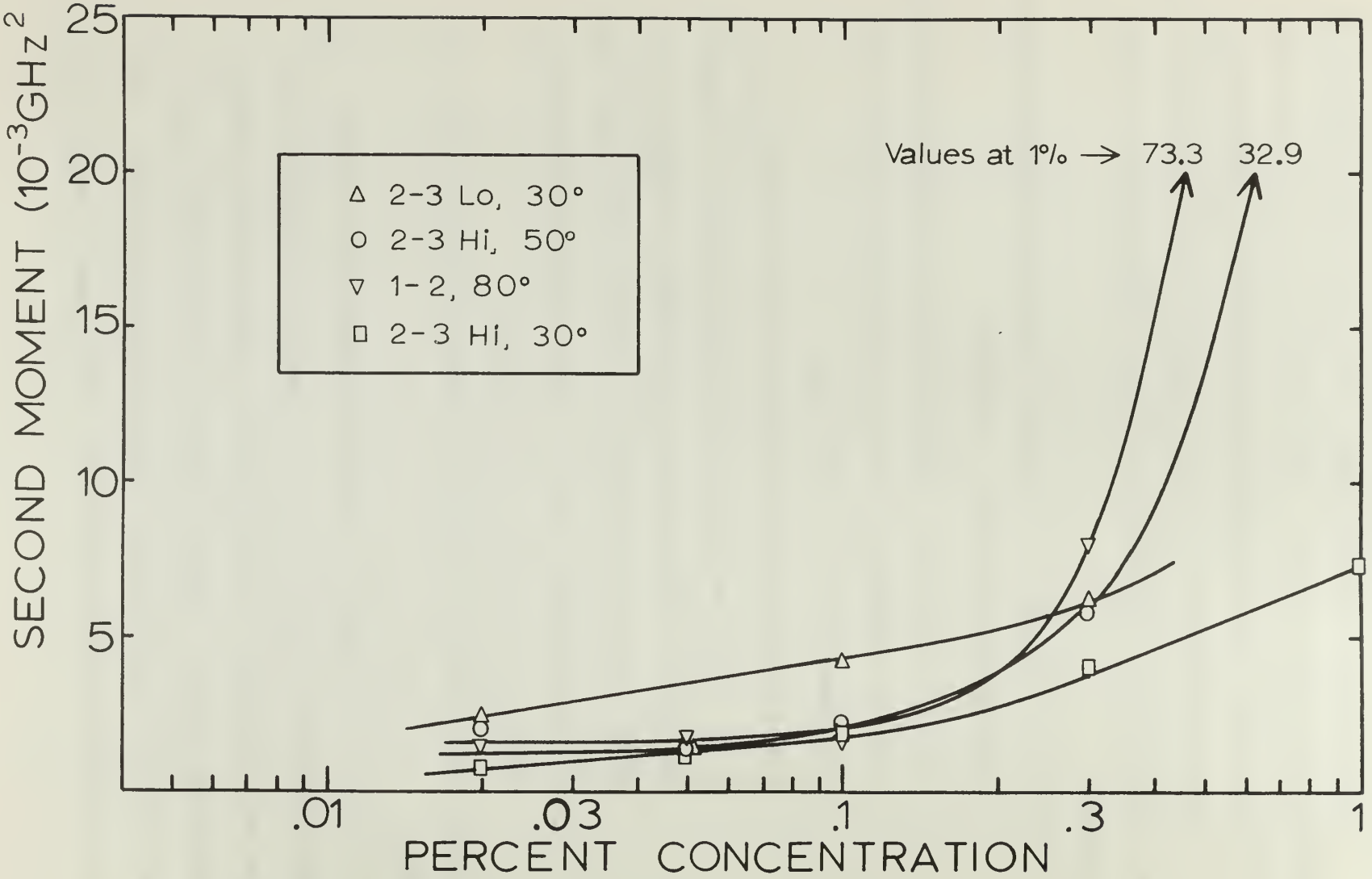

Fig. 6-1. APR second moments vs. Cr concentration

terminated somewhere in the wings or $\langle \Delta\nu^2 \rangle$ diverges), where $\langle \Delta\nu^2 \rangle = 1.35\epsilon^2$. They then showed that neither of these moments is large enough to account for the dipolar part of the theoretical value. In point of fact, however, the line is neither Gaussian nor Lorentzian, so we can consider their values of $\langle \Delta\nu^2 \rangle$ to be just an estimate.

Grant and Strandberg have done a study on line shape in ruby and have inferred most of the second moment is not present in the observable line. Our measurements indicate that this is indeed the case. In the following, we will show how to estimate the size of the interactions involved in a resonance line; then, we will compare the measured widths with theory; and finally, we will try to calculate the second moment by summing only the interactions from neighbors outside a certain radius.

We first demonstrate that the overall width of a resonance line, from where the line is first measurable to where the line returns to zero, is of the order of the largest ion-ion interactions that are causing the shape. For example, consider two identical uncoupled spin ½ particles in a coupled representation. There will be three energy levels: one at +E corresponding to both spins up (++), one at -E corresponding to both spins down (--), and two degenerate levels at zero energy corresponding to up-down (+-) and down-up (-+). Only one transition of energy E is observed from this system, if we discount double spin flips.

We next ask the effect of turning on a small amount of coupling between these particles, say of the form $S_{z1}\ S_{z2}$. Since the Hamiltonian matrix is still diagonal, the change in energy can be found simply by forming matrix elements of the form $\langle a | S_{z1}\ S_{z2} | a \rangle$ and noticing that while the (++) and (--) states both move up a small amount Δ, the degenerate states move down by Δ. There are now two transitions of size $E + 2\Delta$ and

$E - 2\Delta$, respectively; our original transition has "broadened" into a line of overall width 4Δ.

One can also suppose a small off-diagonal coupling of the form $S_{+1} S_{-2} + S_{-1} S_{+2}$ between our original uncoupled particles. In this case, we must rediagonalize our Hamiltonian since the perturbation is between degenerate levels, but the end result is similar: the degenerate levels are mixed, one moving up by Δ, the other moving down by Δ. The original transition at E now consists of two lines at $E + \Delta$ and $E - \Delta$; the "width" is thus 2Δ.

Of course, this simple analysis cannot be taken too far. It is not the interaction of just ions i and j that causes broadening in a large crystal; it is one of the states composed of all the mutually interacting ions of the crystal that yields a resonant frequency different from the single ion frequency. Consequently, when we say that the interaction between ions i and j appears $\Delta\nu$ away from the main resonance frequency, we can expect only order of magnitude accuracy.

We define, then, the "full-width" of a line to be the distance in frequency from where the signal is first detectable above the noise to the center of the line. We also assume that if two Cr ions interact with an energy ϵ, they will produce a displaced line at frequency $\Delta\nu = \epsilon/h$ away from the single ion frequency. In this sense, a measure of the full-width of an observed line gives us a criterion for determining which interactions are contributing to the observable line.

The full-widths of our lines are given in Table 6-1; we note that the full-widths vary from 1135 MHz down to 85 MHz. In order to compare these values to actual interactions, we calculate first the dipolar, and then the exchange, contributions to the second moment.

Table 6-2 is a summary of the dipolar contribution B_k^2 from each nearest neighbor for the first 20 nearest neighbors. It is obvious that the individual contributions of many of the neighbors is more than the total observed second moment itself.

An estimate of the size of the exchange $\tilde{A}_k$ has been given by Statz, et al.[25]; they quote a value of $(1.17 \pm .15) \times 10^4$ GHz for the first neighbor at 2.73A and about 15 GHz at 5.73A (eleventh nearest neighbor). The contributions to $\Sigma \tilde{A}_k^2$ are then 1.37×10^8 GHz^2 and 225 GHz^2, respectively, for these ions. The contrast between theory and experiment here is even more drastic than with the dipolar case, the difference being many orders of magnitude.

	Ruby Number				
	2	3	4	5	6
2-3 Hi, 50^o	192	138	171	266	620
2-3 Hi, 30^o	85	120	171	201	1135
2-3 Lo, 30^o	146	92	216	259	--
1-2, 80^o	129	107	122	230	880

Table 6-1. Full-widths of APR lines. Widths are from beginning of line to center.

Neighbor	Number	r, Å	θ, deg	B_k^2, GHz^2
0	1	--	--	--
1	1	2.728	180	58.9
2	3	2.804	101.6	9.48
3	3	3.180	59.6	.335
4	3	3.498	51.8	.072
4'	3	3.498	128.2	.072
5	1	3.767	0	8.49
6	3	4.758	90	.516
6'	3	4.758	90	.516

Table 6-2. Dipolar contribution of the second moment from each of nearest 20 neighbors. (After ref. 14 and 24). The sum of B_k^2 over all neighbors is 107 GHz^2.

The picture that emerges is now fairly clear. The theoretical second moment as we have calculated it is correct, but the contribution of the near neighbors to this moment is so immense that the transitions caused by these interactions lie in the far wings of the line and are unmeasured. For instance, the nearest neighbor, which lies only 2.73A away from the origin on the z-axis, has an exchange contribution which is 10^7 times bigger than the observed moment; furthermore, its dipolar contribution is, in itself, 10 times larger than the measured value. Indeed, for the first few nearest neighbors, the exchange coupling is so strong that the ions form pairs and tend to produce pair spectra which are quite independent of the single ion line. There is, in fact, a considerable literature built up by workers trying to locate the spectra of these pairs, not without some success[25-27]. For our purpose, however, which is to explain the observed second moments, it is obvious

that we must exclude such pairs from the summations over neighbors.

In order to get a quantitative understanding of the observed line, we are faced with a dilemma. We know we must exclude the near neighbors in our summations and sum only outside some radius r_o; also, to avoid circular reasoning, we must choose r_o without reference to the second moment. If, instead of calculating the second moment (which is insensitive to line structure), we were able to calculate the exact line shape by knowing which atoms contribute to each part of the line, our approach would be obvious. Lacking this straight-forward situation, we resort to the following technique.

We assume that if a Cr ion interacts with a neighbor at radius r such that the interaction strength is greater than the full-width of the line, then that interaction is not being observed and must, consequently, be excluded from our summation. By matching the full-width of a line to the interaction size, we can therefore arrive at a cutoff radius for each term in our second moment.

Obviously, this argument is not without a certain amount of circularity; we use it only as a last resort for determining r_o. We can therefore expect no better than order of magnitude agreement between our measured and calculated value, especially insofar as we will have to make certain assumptions about the relatively unknown exchange energies.

We will choose two radii: r_e is that radius outside of which we will sum the exchange contribution, and r_d is that radius outside of which we will sum the dipole contribution. Since r_e and r_d will turn out to be fairly large, we will perform the sums by integration outside of these radii. We start with the exchange part.

Since the data on exchange is meager, we have fitted the previously quoted two values of Statz, et al.[25] to the equation

$$|\tilde{A}(r)| = \frac{C}{r^n}$$

where $C = 9.93 \times 10^7$ GHz-A^9, and $n = 9.00$. This is, we should point out, a very arbitrary choice for $\tilde{A}$ at all radii. Mollenauer and Schalow[27] have measured $\tilde{A}$ for the first four nearest neighbors; their values do not obey an r^{-n} law. But even a knowledge of $\tilde{A}(r)$ for near neighbors does little to help us predict $\tilde{A}$ for the far neighbors. The radial dependence of $\tilde{A}$, for instance, depends critically on how many oxygen ions lie between the Cr ion pair; also, one can obtain both positive or negative values for $\tilde{A}$, indicating ferromagnetic or antiferromagnetic coupling, respectively. ($\tilde{A}^2$, however, is always positive.)

We now choose the transition for our calculation: 2-3 Hi at 50^o in sample 6 (1% Cr concentration). This line has a full-width of 620 MHz (Table 6-1) and a second moment $\langle \Delta\nu^2 \rangle = .036$ GHz^2 (Fig. 6-1). The exchange cutoff radius r_e, obtained by setting $|\tilde{A}| = 620$ MHz and solving for r, is 8.16A. This is a large radius-- a sphere of this radius contains some 40 neighbors-- so we will approximate the summation outside r_e by the integral

$$\sum_{r_e}^{\infty} |\tilde{A}(r)|^2 \approx \int_{r_e}^{\infty} \tilde{A}^2 \rho \, 4\pi r^2 dr$$

where ρ = number of ions per unit volume = .0574 atom/A^3 and $A = C/r^n$ as before. The result is 10.1 GHz^2.

The next sum is the dipole sum. We recall from Chapter II that the dipole-dipole energy for neighbor k is

$$B_k = \frac{-3g^2\beta^2(3\gamma^2 - 1)/2}{r_k^3}$$

Ignoring the directional factor and setting B_k = 620 MHz, we can solve for the dipole cutoff radius r_d and get r_d = 6.30A. The summation over B_k^2 then reintroduces the directional factor:

$$\Sigma B_k^2 = \int_o^{2\pi} d\phi \int_o^{\pi} \sin\theta \, d\theta \int_{r_d}^{\infty} \rho B_k^2 r^2 \, dr$$

The factor $(3/2 \gamma_k^2 - \frac{1}{2})^2$ is thus averaged over all directions and we get $\Sigma B_k^2 = 4.63 GHz^2$.

The last sum is $\Sigma \tilde{A}_k B_k$, which vanishes because the angular average of $3/2 \gamma_k^2 - \frac{1}{2}$ is zero.

The moment expression is, then,

$$\langle \Delta\nu^2 \rangle = \frac{f}{4} (\alpha \Sigma \tilde{A}_k^2 + \delta \Sigma B_k^2)$$

Inserting f = .01, α = 9.47, and δ = 1.37 for this transition (see Table 2-1) we arrive at $\langle \Delta\nu^2 \rangle$ = .255 GHz^2 as an estimate of the second moment. Although our measured moment of .036 GHz^2 is some 7 times smaller than this, we feel that we have arrived at order of magnitude agreement with experiment.

Another feature of the second moments of high concentration is their variability from transition to transition. In view of our inability to accurately predict these moments, it is difficult to assess the cause of this variability. If we assume that $\Sigma \tilde{A}_k^2$, $\Sigma \tilde{A}_k B_k$ and ΣB_k^2 are constant for all lines, as theory predicts, then we should be able to solve for the sums using three moment equations and the known coefficients. Hopefully, the angular dependence would then be due to the angular variation of α, β, and δ. We have attempted this fit unsuccessfully; in fact, we have even obtained large negative, and therefore uninterpretable, values for ΣB_k^2.

We could postulate that variation is caused by a wandering of the crystal c-axis as we proceed along the sample rod axis. Wenzel and Kim[28] have discussed this effect in order to explain the low-concentration linewidth; in our case, it will affect those transitions whose angular variation $dH/d\theta$ is large. From Fig. 2-4, we see that the transitions 1-2 at 80° and 2-3 Hi at 50° are most eligble for this type of broadening. We have calculated that, for a half-width of 300 MHz, the c-axis would only have to wander a degree or so, which for a high concentration ruby (1%) is not at all unreasonable. We feel, however, that while these transitions are indeed the larger observed ones at 1%, a careful angular study would have to be made to confirm this explanation.

The third feature of the second moment curves is the residual moment of .002 GHz^2 at low concentration. This effect has been observed as a residual half-width in EPR measurements, and Grant and Strandberg[23] have reviewed the various explanations. More recently, Wenzel and Kim[28] have had some success on the problem by using various models for crystalline imperfections. A calculation of the EPR second moments at low concentration has been made by Laurance, McIrvine and Lambe[24], who assume that the residual width is due to hyperfine interaction with the neighboring aluminum nuclei. While our second moments are for APR, their value of .000029 GHz^2 is orders of magnitude too small.

Inasmuch as the experimental second moments for APR have resisted quantitative interpretation, we confine our EPR results to the half-widths of the transitions only. (By half-width is meant the full width of the line at the half power point.) Figure 6-2 gives the EPR

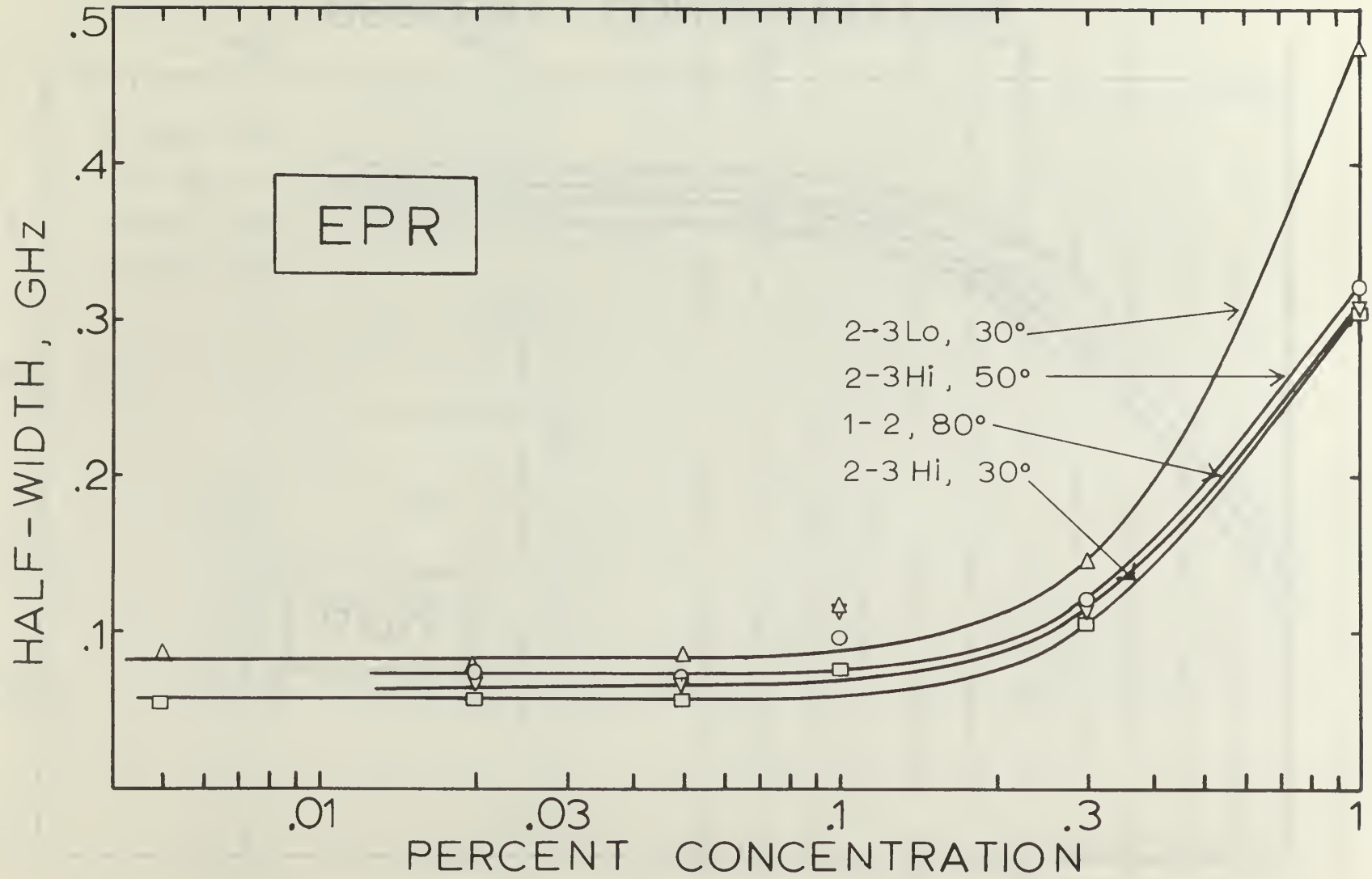

Fig. 6-2. EPR half-widths (full width at half power) vs. Cr concentration

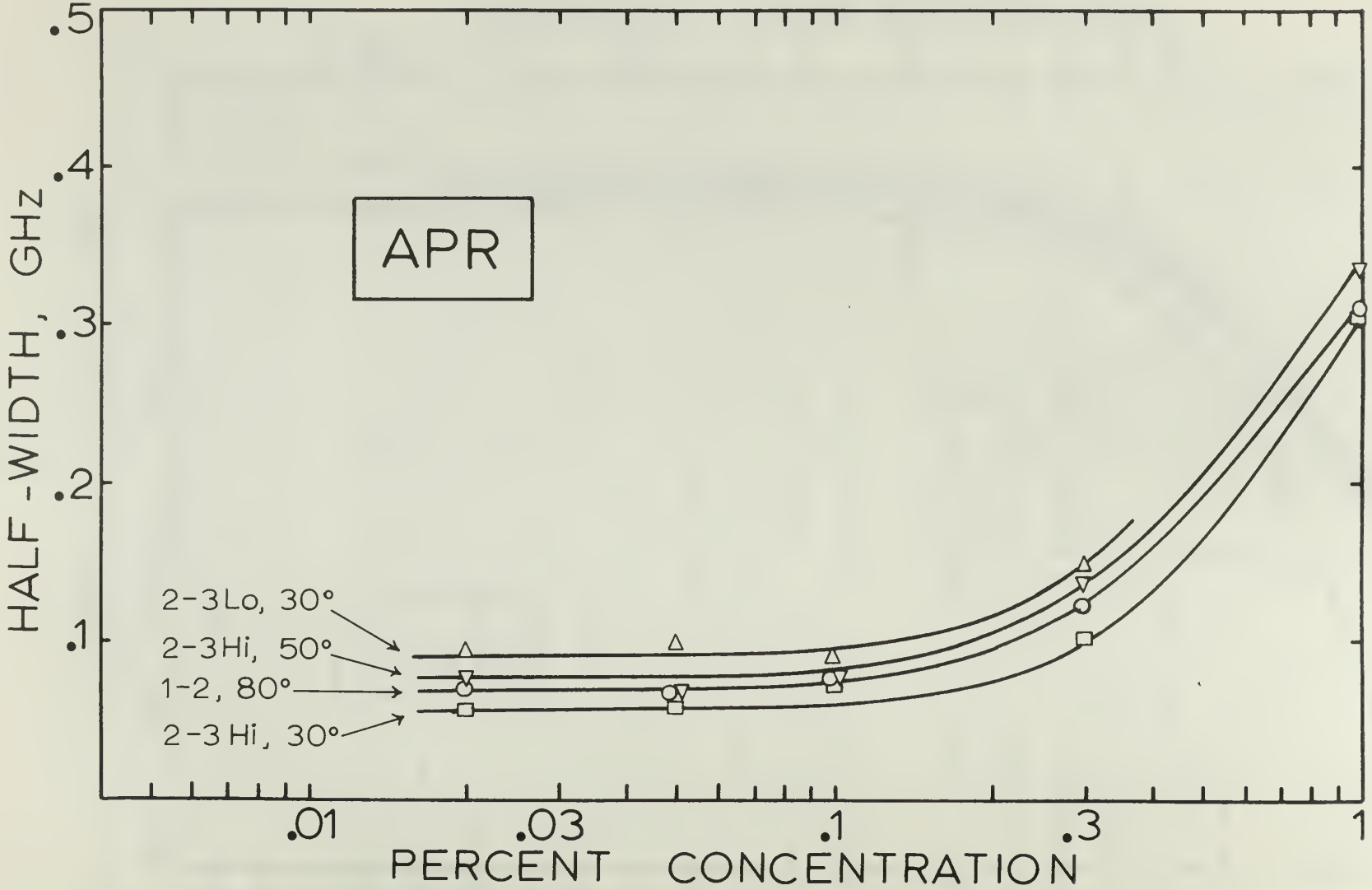

Fig. 6-3. APR half-widths (full width at half power) vs. Cr concentration

half-width; Fig. 6-3 presents the corresponding APR half-widths. The curves are quite similar. Both APR and EPR half-widths are about 320 MHz at 1% concentration and they both decrease to approximately 70 MHz at .05% concentration and lower. The angular dependence of the lines is qualitatively the same: almost no angular dependence at 1%, while at low concentration the ordering in magnitude of the transitions is the same. Table 6-3 compares the half-widths at high and low concentration. We feel that the differences that occur are quite minor, but that a systematic study of linewidths versus angle would be useful to confirm this in detail. As a further complication, it should also be borne in mind that the half-width measures the central part of the line, so that while the second moment deals with the distant neighbors of a Cr ion, the half-width is caused by neighbors even further away. A theory of half-widths is therefore even more difficult to construct.

	.02%		1%	
Transition	EPR, MHz	APR, MHz	EPR, MHz	APR, MHz
2-3 Hi, 50^{o}	66	67	308	308
2-3 Hi, 30^{o}	56	56	308	315
2-3 Lo, 30^{o}	78	91	470	---
1-2 at 80^{o}	72	67	321	336

Table 6-3. Half-widths of EPR and APR lines at two concentrations. Half-widths are the full widths at half-power points.

We now finish this section with a summary:

1. We have rederived the general second moment formula of Pryce and Stevens and have shown that it is also applicable to APR. We have then applied this theory to ruby and arrived at an expression for $\langle \Delta\nu^2 \rangle$ in terms of angular dependent matrix elements, Cr concentration, and sums over $\tilde{A}_k$ and B_k, the exchange and dipolar parts, respectively, of the Cr-Cr interaction.
2. APR and EPR lineshapes have been measured for four transitions as a function of Cr concentration. APR second moments have been experimentally determined for the first time; APR and EPR half-widths have been compared.
3. The EPR and APR half-widths quantitatively appear to be the same.
4. At low concentration, the second moment is concentration independent and is much larger than the theoretical value predicted by Laurance, et al.[24]
5. At high concentration, the APR second moment is much too small if all neighbor contributions are taken into account. We have shown that the nearer neighbor contributions to the second moment lie in the unmeasured wings of the line, thereby confirming previous predictions. A rough calculation has shown that qualitative agreement can be achieved when neighbors out to about 6A and 8A for the dipolar and exchange parts of the interactions, respectively, are excluded.

BIBLIOGRAPHY

1. E. Zavoisky, J. Phys. USSR 9, 245 (1945).

2. J.H. Van Vleck, Phys. Rev. 74, 1168 (1948).

3. M.H.L. Pryce and K.W.H. Stevens, Proc. Phys. Soc. A63, 36 (1950).

4. E. Ishiguro, K. Kambe, and T. Usui, Physica 17, 310 (1951).

5. E.H. Jacobsen, N.S. Shiren, and E.B. Tucker, Phys. Rev. Letters 3, 81 (1959).

6. S.A. Altshuler, B.I. Kochelaev, and A.M. Leushin, Soviet Phys. - Uspekhi 4, 880 (1962).

7. R. Loudon, Phys. Rev. 119, 919 (1960).

8. H.C. Meyer, J.S. Bennett, P.L. Donoho, and A.C. Daniel, Bull. Am. Phys. Soc. 11, 202 (1966).

9. G.A. Weeks, PhD Thesis, Naval Postgraduate School, 1964 (unpublished).

10. C. Kittel and E. Abrahams, Phys. Rev. 90, 238 (1953).

11. K. Kambe and T. Usui, Prog. Theoret. Phys. 8, 302 (1952).

12. M. McMillan and W. Opechowski, Can. J. Phys. 38, 1168 (1960).

13. A. Messiah, Quantum Mechanics (John Wiley & Sons, New York, 1961) Vol I, p. 262.

14. R.W.G. Wyckoff, Crystal Structures (Interscience Publishers, New York, 1948), 2nd ed., Vol II, p. 6.

15. A.A. Manenkov and A.M. Prokhorov, Soviet Physics - JETP 1, 611 (1955).

16. For example: B. Bleaney and K.W.H. Stevens, Rep. Prog. Phys. 16, 107 (1953).

17. J.E. Geusic, Phys. Rev. 102, 1252 (1956).

18. A.E. Siegman, Microwave Solid State Masers (McGraw-Hill Book Co., Inc., New York, 1964).

19. C.M. Verber, H.P. Mahon, and W.H. Tantilla, Phys. Rev. 125, 1149 (1962).

20. J.G. Stephenson, Electronics, 18 Jan 1963, p. 46.

21. G. Feher, Bell System Tech. J. 36, 449 (1957).

22. A.A. Manenkov and V.B. Fedorov, Soviet Physics - JETP 11, 751 (1960).

23. W.J.C. Grant and M.W.P. Strandberg, Phys. Rev. 135, A727 (1964).

24. N. Laurance, E.C. McIrvine, and J. Lambe, J. Phys. Chem. Solids 23, 515 (1962).

25. H. Statz, L. Rimai, M.J. Weber, G.A. de Mars, and G.F. Koster, J. Appl. Physics 32, 218S (1961).

26. A.A. Kaplyanskii and A.K. Przhevuskii, Soviet Phys. - Solid State 9, 190 (1967).

27. L.F. Mollenauer and A.L. Schawlow (to be published).

28. R.F. Wenzel and Y.W. Kim. Phys. Rev. 140, A1592 (1965).

APPENDIX

CRYSTAL BONDING

Inasmuch as considerable time and effort were spent in perfecting a technique for bonding transducers, we present in this appendix our final method. We do not claim that this is the only successful approach, nor do we even claim that all of our steps are absolutely essential. We do, however, assert that the method was repeatedly successful. The procedure is set forth in step-by-step form:

1. Clean the quartz and ruby faces. The ruby could be moved with ordinary tweezers; however, in order to prevent breakage of the ultra-thin quartz plate, we made up a set of thin teflon tweezer tips for gentler handling. (A vacuum tweezer was also tried, but this was unsuccessful.) The cleaning solutions are:
   a) Concentrated nitric acid - 5 min.
   b) Flush with distilled water.
   c) Detergent and water - scrub with Q-tip or ultrasonic cleaner for 5 min. If the quartz is placed on a wet tissue over a flat glass surface, it can be safely scrubbed with a Q-tip. An ultrasonic cleaner can break thin quartz plates.
   d) Flush with distilled water.
   e) Reagent grade acetone - scrub for 5 min.
2. Prepare the bonding material. We used Nonaq Stopcock Grease (Fisher Scientific Co.). Several bottles were stored in an ordinary refrigerator freezer at all times. Since Nonaq absorbs water from the air, the bottle should never be left open.

a) Place fresh blob of Nonaq on a glass slide and cover with watch glass.

b) Put the slide on a small electric hotplate set to about 210°C. Heat till granularity disappears - about 5 min. This step is absolutely essential.

3. Just prior to bonding, give quartz and ruby one last wipe with reagent acetone. Make sure no drying marks remain on either crystal.

4. With a glass rod, remove a small drop of Nonaq from the heated blob. Place drop on ruby face. Invert ruby and pick up quartz.

5. Place quartz-ruby in a jig so that vertical pressure can be applied to the quartz. We used a staking tool; on the end of the plunger rod was a cylinder of silicon rubber, slightly smaller in diameter than the quartz. Press with about 150g for 15 min. Too long a time will cause vacancies in the bond material. The best bonds occur when the Nonaq spreads to edge of quartz but no further.

6. Remove bond and check for uniformity by observing fringes, visible by an fluorescent desk lamp or, to a lesser extent, by incandescent light.

7. Check on 500 MHz test rig. An even pulse envelope shape is indicative of good uniformity. The bond is now ready for use.

8. Cooling down to low temperature must be slow in order to give the cold Nonaq a chance to flow. Do not evacuate the sample space, however: Nonaq tends to bubble. Our cooldown times were about 12 hours.

9. There is a large amount of art in successful bonding. We have had difficulty bonding on humid days, and sometimes a half-full bottle of Nonaq had to be discarded. On the other hand, what we thought were rather poor quality bonds occasionally gave excellent echoes. Trial and error sometimes seems to be the only answer.

INITIAL DISTRIBUTION LIST

		No. Copies
1.	Defense Documentation Center Cameron Station Alexandria, Va. 22314	20
2.	Library Naval Postgraduate School Monterey, California 93940	2
3.	Physics Department Library Naval Postgraduate School Monterey, California 93940	1
4.	Mr. Peter P. Crooker Lincoln Laboratory Lexington, Mass.	5
5.	Prof. E.C. Crittenden, Jr. Dept. of Physics Naval Postgraduate School Monterey, California 93940	1
6.	Prof. O.B. Wilson, Jr. Dept. of Physics Naval Postgraduate School Monterey, California 93940	1
7.	Prof. G.E. Schacher Dept. of Physics Naval Postgraduate School Monterey, California 93940	1

DOCUMENT CONTROL DATA - R&D

(Security classification of title, body of abstract and indexing annotation must be entered when the overall report is classified)

1. ORIGINATING ACTIVITY (Corporate author)	2a. REPORT SECURITY CLASSIFICATION
Naval Postgraduate School	Unclassified
	2b. GROUP

3. REPORT TITLE

Phonon and Photon Paramagnetic Resonance Lineshape in Ruby

4. DESCRIPTIVE NOTES *(Type of report and inclusive dates)*

Ph D Thesis, Physics

5. AUTHOR(S) *(Last name, first name, initial)*

Crooker, Peter P.

6. REPORT DATE	7a. TOTAL NO. OF PAGES	7b. NO. OF REFS
December 1967	80	28

8a. CONTRACT OR GRANT NO.	9a. ORIGINATOR'S REPORT NUMBER(S)
b. PROJECT NO.	
c.	9b. OTHER REPORT NO(S) *(Any other numbers that may be assigned this report)*
d.	

10. AVAILABILITY/LIMITATION NOTICES

GRL 11/69

[redacted]

This document has been approved for public release and sale; its distribution is unlimited.

11. SUPPLEMENTARY NOTES	12. SPONSORING MILITARY ACTIVITY
	Naval Postgraduate School

13. ABSTRACT

Electron paramagnetic resonance (EPR) and acoustic paramagnetic resonance (APR) lineshapes have been measured for four transitions in ruby at 5.924 GHz. Cr concentrations varying from .005% to 1% were used. Second moments were calculated from the APR lines; half-widths were calculated from both EPR and APR lines. A theory is presented which yields the second moment in terms of sums over exchange and dipole-dipole interactions between Cr pairs. It is shown that the theory predicts moments much larger than measured due to the fact that the stronger Cr-Cr interactions lie outside the observed line. A qualitative calculation of the moment from the known interactions supports this conclusion. Finally, half-widths for both APR and EPR lines are compared and shown to be equal.

DD FORM 1 JAN 64 1473

14. KEY WORDS	LINK A		LINK B		LINK C	
	ROLE	WT	ROLE	WT	ROLE	WT
Ruby						
Acoustic Resonance						
Magnetic Resonance						
Lineshape						